EFFICIENT PARAMETER MAPPING FOR MAGNETIC RESONANCE IMAGING

A THESIS SUBMITTED TO
THE GRADUATE SCHOOL OF ENGINEERING AND SCIENCE
OF BILKENT UNIVERSITY
IN PARTIAL FULFILLMENT OF THE REQUIREMENTS FOR
THE DEGREE OF
MASTER OF SCIENCE
IN
ELECTRICAL AND ELECTRONICS ENGINEERING

By
Kübra Keskin
July 2019

Efficient Parameter Mapping for Magnetic Resonance Imaging
By Kübra Keskin
July 2019

We certify that we have read this thesis and that in our opinion it is fully adequate, in scope and in quality, as a thesis for the degree of Master of Science.

Tolga Çukur(Advisor)

Ergin Atalar

Yeşim Serinağaoğlu Doğrusöz

Approved for the Graduate School of Engineering and Science:

Ezhan Karaşan
Director of the Graduate School

ABSTRACT

EFFICIENT PARAMETER MAPPING FOR MAGNETIC RESONANCE IMAGING

Kübra Keskin
M.S. in Electrical and Electronics Engineering
Advisor: Tolga Çukur
July 2019

Balanced steady-state free precession (bSSFP) is a magnetic resonance imaging (MRI) sequence that enables high signal-to-noise ratios in short scan times. However, it has elevated sensitivity to main field inhomogeneity, which leads to banding artifacts near regions of relatively large off-resonance shifts. To suppress these artifacts, multiple bSSFP images of the same anatomy are commonly acquired with a set of different RF phase-cycling increments. Joint processing of phase-cycled acquisitions has long been employed to eliminate banding artifacts due to field inhomogeneity. Multiple bSSFP acquisitions can be further used for parameter mapping by exploiting the signal model of phase-cycled bSSFP. While model based approaches for mapping are effective, they often need a large number of acquisitions, inherently limiting scan efficiency. In this thesis, we propose a new method for parameter mapping with improved efficiency and accuracy in phase-cycled bSSFP MRI. The proposed method is based on the elliptical signal model framework for complex bSSFP signals; and introduces an observation about the signal's geometry to the constrained parameter mapping problem, such that the number of unknowns and thereby the required number of acquisitions can be reduced. It also leverages dictionary-based identification to improve estimation accuracy. Simulated, phantom and in vivo experiments demonstrate that the proposed method enables improved parameter mapping with fewer acquisitions.

Keywords: Magnetic resonance imaging (MRI), balanced SSFP, phase-cycling, parameter mapping, ellipse fitting, constrained optimization.

ÖZET

MANYETİK REZONANS GÖRÜNTÜLEME İÇİN VERİMLİ PARAMETRE HARİTALAMASI

Kübra Keskin
Elektrik ve Elektronik Mühendisliği, Yüksek Lisans
Tez Danışmanı: Tolga Çukur
Temmuz 2019

Dengeli kararlı-durum serbest devinim (bSSFP), kısa görüntüleme sürelerinde yüksek SNR sağlayan bir manyetik rezonans görüntüleme (MRG) sekansıdır. Fakat, ana manyetik alan eşitsizliklerine karşı hassaslığı bulunmaktadır, bu hassaslık rezonans dışı frekans kaymalarının görece fazla olduğu bölgelerde bant artefaktlarına sebep olur. Bu artefaktları bastırmak için genellikle bir dizi farklı RF faz çevrimi artırımı kullanılarak aynı anatominin birden fazla bSSFP görüntüsü elde edilir. Faz-çevrimli bSSFP taramalarının birlikte işlenmesi, manyetik alan eşitsizlerinden kaynaklanan bant artefaktlarını bastırmak için uzun zamandır kullanılmaktadır. Çoklu faz-çevrimli bSSFP taramaları, faz-çevrimli bSSFP sinyal modelinden faydalanılarak parametre haritalaması için de kullanılabilir. Model tabanlı bu yaklaşımlar etkili olsa da genellikle çok sayıda veri taraması yapılmasına ihtiyaç duyar, bu yüzden de tarama verimliliğini sınırlar. Bu tezde faz-çevrimli bSSFP ile parametre haritalamayı artırılmış verimlilik ve doğruluk ile yapmak için yeni bir yöntem önerilmiştir. Önerilen yöntem, karmaşık bSSFP sinyalleri için oluşturulan eliptik sinyal modeline dayanır; ve sinyalin geometrisi ile ilgili bir gözlemi kısıtlı parametre haritalaması problemine dahil eder, böylece bilinmeyenlerin sayısı ve bu sayede problem için gereken tarama sayısı azaltılabilir. Bu yöntem, tahminlerin doğruluğunu artırmak için sözlüğe dayalı bir tanımlama işlemi de kullanmaktadır. Yapılan benzetimler, fantom ve in vivo deneyler, önerilen yöntemin daha az tarama ile parametre haritalamasına izin vererek tarama verimliliğini artırdığını göstermektedir.

Anahtar sözcükler: Manyetik rezonans görüntüleme (MRG), dengeli karalı-durum serbest devinim (bSSFP), faz-çevrimi, parametre haritalaması, elips uydurumu, kısıtlı eniyileme.

Acknowledgement

I would first like to thank my thesis advisor Prof. Tolga Çukur for his continuous support and guidance. His door was always open whenever I encountered a problem, or had a question about my research. He always believed in me, and encouraged me when I slowed down. I feel very lucky to have him as my advisor.

I would like to thank Prof. Ergin Atalar for his informative and thought provoking classes, and also for establishing an open and productive research environment where we can benefit from the advantages being offered by UMRAM. I would also like to thank Prof. Yeşim Serinağaoğlu Doğrusöz for her valuable comments and kindly accepting to be in my thesis committee. I also want to express my gratitude to Prof. Orhan Arıkan, and Prof. Emine Ülkü Sarıtaş for all their precious advice.

I also acknowledge the financial support of The Scientific and Technological Research Council of Turkey (TÜBİTAK) during my graduate study under the project 117E171.

Throughout two years I had a chance to meet and work with very great people. I am grateful to Uğur Yılmaz for answering every question I had about MRI. I want to thank Toygan and Safa for helping me out with my MRI experiments, Salman for helping me in every respect in the lab, my fellow class mates Ömer and Bilal, my fellow lab mates Ecrin, Özgür, Emin, Muzaffer, Batu, Kaan, Mahmut, Erdem and Cemre, my fellow schoolmates Büşra, Talha and Osman, and many other great people I met in Bilkent for cheering this period up.

I also feel very fortunate to have my dear friends Büşra, Fatma, Büşra and Esra, with whom I share lots of wonderful memories for many years.

I wish to give thanks to my parents Mümine and Ahmet, my brother Furkan and his wife Dudu for their endless caring and support throughout my life.

Finally, I would like to share my deepest appreciation to my fiance İbrahim

Kurban for always standing by me, helping me to get through hardships, and motivating me in every aspect of my life especially in the process of researching and writing this thesis. This accomplishment would not have been possible without all these people.

Contents

List of Figures

List of Tables

List of Abbreviations

BSS	Bloch-Siegert Shift
bSSFP	Balanced Steady State Free Precession
CELF	Constrained Ellipse Fitting
CSF	Cerebrospinal Fluid
DESPOT1	Driven Equilibrium Single Pulse Observation of T1
DESPOT2	Driven Equilibrium Single Pulse Observation of T2
ESM	Elliptical Signal Model
FOV	Field-of-View
GEP	Generalized Eigenvalue Problem
GM	Gray Matter
GS	Geometric Solution
IR	Inversion Recovery
LORE-GN	Linearization for Off-Resonance Estimation-Gauss Newton
MAPE	Mean Absolute Percentage Error
MRI	Magnetic Resonance Imaging
NMR	Nuclear Magnetic Resonance
RF	Radio Frequency
ROI	Region of Interest

SE	Spin Echo
SNR	Signal-to-Noise Ratio
TE	Echo Time
TR	Repetition Time
TSE	Turbo Spin Echo
T1	Relaxation Parameter of Longitudinal Magnetization
T2	Relaxation Parameter of Transverse Magnetization
WM	White Matter

Chapter 1

Introduction

Magnetic Resonance Imaging (MRI) is a commonly used imaging modality. Since it has been founded, it gains great attention, and the research being conducted for MRI grows rapidly. This is because; it holds a great potential as a non-invasive and safe diagnostic tool, and it is programmable so that variety of image contrasts, quantitative maps, and information can be extracted with modifications of the system parameters. This thesis focuses on the quantitative parameter mapping part of the MRI, and introduces an efficient parameter mapping method by using the balanced steady state free precession (bSSFP) sequence. Main contribution of this thesis is to demonstrate that by introducing a new constraint into the parameter mapping problem, required number of scans for obtaining the parameter maps can be reduced, and also by applying a dictionary-based refinement, accuracy of the maps can be improved.

1.1 Outline of the Thesis

Chapter 2 provides an overview of the background information for MRI. Basic principles of MRI covering magnetic fields, spin movements, excitation, relaxation, spatial encoding, signal formation and pulse sequences are briefly described. Then, the bSSFP sequence utilized in this thesis is further explained to provide a foundation for the method proposed in chapter 3. For this purpose, types of SSFP sequences are explained, bSSFP signal equation is derived, and phase-cycled bSSFP is mentioned.

Chapter 3 introduces a novel method enabling parameter mapping with less number of data acquisitions. Works in the literature related to this study is reviewed, the theory including the derivation of proposed constrained parameter mapping problem is provided, simulated, phantom and in vivo experiments are explained, results and comparisons of the proposed method are demonstrated and discussed. Finally, Chapter 4 summarizes the findings of this thesis.

Chapter 2

Background

In this chapter, an overview of basic concepts in Magnetic Resonance Imaging (MRI) is introduced. Then, the balanced steady state free precession (bSSFP) sequence is explained further as it constitutes an important part of this study.

2.1 MR Overview

Basics of magnetic resonance imaging (MRI) is shortly explained in this section. An overview to understand how an image is formed with MR is provided, including physics, spin movements, applied magnetic fields, relaxation, Bloch equation, signal formation and main pulse sequences.

2.1.1 Main Field B_0 and RF Field B_1

When a strong external field (B_0) is applied, nuclei of a sample, that are normally placed in random orientations, are aligned with the same or opposite directions of the applied B_0 field. However, in overall B_0 field's effect is seen as a net magnetization towards the B_0 field direction which is also called longitudinal

direction (or z-direction). Other two directions perpendicular to each other in three dimensional space form the transverse plane (or xy-plane).

Also, as a result of B_0 field, resonance is observed in nuclear spins at the Larmor frequency which is simply multiplication of gyromagnetic ratio γ which is approximately 42.58 MHz/Tesla for the ^1H atom and the strength of B_0 field. If they are excited by a magnetic field tuned to spins' Larmor frequency, they precess about the field at this certain frequency and a signal out of these spins is produced. The magnetic field that excites the spins at their resonance frequency is called radio frequency (RF) field or B_1 field. If an RF field applied in transverse plane, magnetization vectors produced by spins at B_0 field rotate towards the transverse plane by flip angle which is the integral of the RF pulse $B_1(t)$ over time multiplied by the gyromagnetic ratio, and magnetization vectors start to precess at Larmor frequency around the z-axis. Typically duration of the RF pulse is small and strength of the field is really small compared to main field. After the RF pulse, magnetization vectors start to be relaxed and turn back to their initial position aligned with the longitudinal direction while still precessing about the z-axis at Larmor frequency. Since precessing occurs at a specific frequency, reference frame for the magnetization vectors' movements is chosen as the rotating frame. This enables simplified explanations for the movements of the magnetization vectors, and makes magnetization vectors tractable.

2.1.2 Relaxation

Return of the magnetization vectors to their initial direction is characterized by two parameters. One is the recovery time constant of the thermal equilibrium magnetization along the longitudinal direction, therefore it is called longitudinal relaxation time or T_1. Other is the decay time constant of the magnetization vector at transverse plane, so it is called transversal relaxation time or T_2. T_1 and T_2 values are different for tissues, which allows soft tissues to be differentiated among themselves and provides various contrasts in MR images.

2.1.3 Bloch Equation

The differential equation summarizing the previous nuclear magnetic resonance concepts is called Bloch Equation:

$$\frac{\partial \bar{M}}{\partial t} = \bar{M} \times \gamma \bar{B} - \frac{M_x}{T_2}\hat{\mathbf{i}} - \frac{M_y}{T_2}\hat{\mathbf{j}} - \frac{M_z - M_0}{T_1}\hat{\mathbf{k}} \tag{2.1}$$

Here, $\bar{M} = [M_x, M_y, M_z]^T$ is the magnetization vector, and M_0 is the thermal equilibrium. We can see that relaxation time constants are originated from the Bloch equation. If we assume $\bar{B}$ is only along the z-axis, then the Equation 2.1 can be written as:

$$\frac{\partial M_z}{\partial t} = -\frac{M_z - M_0}{T_1}\hat{\mathbf{k}} \tag{2.2}$$

and the solution of this differential equation is

$$M_z(t) = M_0 + (M_z(t=0) - M_0)\exp(-t/T_1) \tag{2.3}$$

where we can see that T_1 characterizes the rate of recovery of the equilibrium magnetization. The same applies to transversal relaxation T_2 when the following differential equation is considered for the magnetization vector at the transverse plane ($\bar{M}_{xy}$):

$$\frac{\partial \bar{M}_{xy}}{\partial t} = -\frac{\bar{M}_{xy}}{T_2} \tag{2.4}$$

Then, the solution below shows that the transversal relaxation time T_2 explains the rate of decay of the magnetization in the transverse plane.

$$\bar{M}_{xy}(t) = \bar{M}_{xy}(t=0)\exp(-t/T_2) \tag{2.5}$$

2.1.4 Signal Formation

Magnetization vectors tilted towards the transverse plane by RF excitation produce signals which then can be collected by receiver coils. However, they could not give any information about spatial location of acquired signals unless spatial

information is encoded with some procedures. Spatial encoding in MRI is done with manipulation of the gradient magnetic fields. Gradient fields are configured such that each imaged area has a particular frequency. Then, the acquired signal becomes the combination of signal strengths of each imaged area at different frequencies. Therefore, the signal strength at specific location can be determined by simply taking the Fourier Transform of the acquired combined signal. Signal collection with MRI can be interpreted as sampling in the Fourier domain, and the space from where the data is collected is called k-space.

Based on the sequence being 2D or 3D, spatial encoding in MRI is carried out by applying different gradient fields. The gradient field applied along the x-axis (G_x) is generally used for frequency encoding which allows signals to be localized by their frequency components. The gradient field applied along the y-axis (G_y) is used for phase encoding which enables location in y-direction to be resolved. Phase encoding corresponds to acquisition of different lines in y-direction of k-space. The gradient field applied along the z-axis (G_z) is used for slice selection when a 2D sequence is employed, however during 3D sequence it is used for phase encoding along the z-direction. Then the acquired MR signal $s(t)$ can be stated as following:

$$s(t) = \int_x \int_y \int_z m(x, y, z) \exp(-i2\pi(k_x(t)x + k_y(t)y + k_z(t)z))\, dx\, dy\, dz \quad (2.6)$$

where $m(x, y, z)$ is the magnetization of an area being imaged, $k_{\{x,y,z\}}(t) = \gamma \int_0^t G_{\{x,y,z\}}(\tau)d\tau$, and some effects that are occurred due to imperfections and therefore change the signal equation are ignored.

2.1.5 Pulse Sequences

There are two types of frequently used main MR sequences based on how many RF pulses are applied and how an echo is formed; spin echo (SE) and gradient echo (GRE). An echo is called spin echo when it is obtained with manipulation of spin movements, and called gradient echo when with manipulation of gradients,

as their names suggest.

2.1.5.1 Spin Echo

Spin echo is obtained when more than one RF pulses are applied such that phases dispersed due to inhomogeneities could fully rephase. Firstly, an excitation with 90 degrees along a direction in the transverse plane (we can assume it is x-axis) is applied, and this tilts magnetization vectors towards the y-axis (Figure 2.1 B). Then, each spin vector starts to dephase as each has different precession frequency (Figure 2.1 C). Later, second excitation with 180 degrees is applied, and this rotates all magnetization vectors about the x-axis (Figure 2.1 E). Following the second RF pulse, each spin vector continues to start precess with their frequencies (Figure 2.1 F). After some time, they come up again and create an echo called spin echo (Figure 2.1 G).

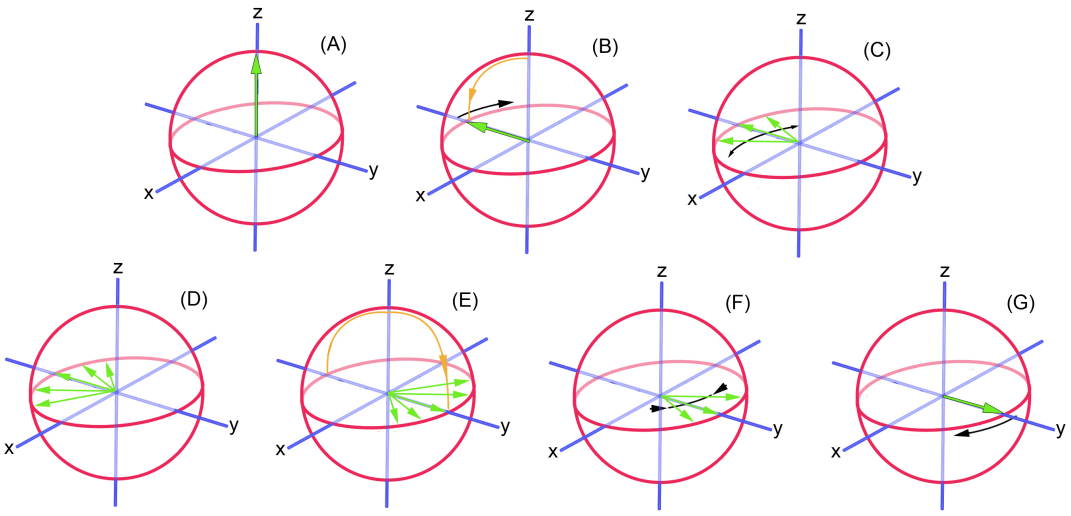

Figure 2.1: An illustration of how an echo is formed with the spin echo

2.1.5.2 Gradient Echo

Gradient echo is formed where integral of the gradient waveform sums up to zero, which is equivalent to crossing over the origin in k-space. It differs from

spin echo as the echo is obtained with an RF pulse and gradient reversal. As there is one excitation pulse, echo can be obtained more rapidly, and thereby echo time (TE) is generally shorter than echo times of spin echo sequences. This is because rapid imaging techniques using short TR and short TE are mostly based on GRE sequences, for example, a rapid imaging sequence steady state free precession (SSFP) is a GRE sequence. However, GRE sequences are more susceptible to artifacts than SE, and phase shifts occurred due to inhomogeneties do not cancel out when echo is formed.

2.2 Balanced Steady State Free Precession

Sequences that steady state responses are observed are called steady state free precession (SSFP). Steady state is formed when a long train of RF excitations with a constant flip angle and short TR is applied to the field, and after some time magnetization vector reaches the steady state. In steady state, the signal is continuous and its amplitude does not die out, since TR is much shorter than longitudinal and transverse relaxation parameters (T_1 and T_2), and therefore this rapid repetitions do not allow transverse magnetization vector to return back their initial states. There are some conditions for this situation to be occurred; TR should be dramatically shorter than T_2, inhomogeneity of the field should remain constant, and phase accumulations due to gradients should not change between repetitions. There are types of SSFP which differ in the way the residual magnetization after a repetition is spoiled; RF-spoiled sequences cancel the transverse magnetization while gradient spoiled sequences average it, and unspoiled fully balanced SSFP recovers it [1]. Therefore, the contrast each sequence provides is variable depending on how the residual magnetization is treated, and other sequence parameters. The highest signal amplitudes over varying range of flip angle for blood and muscle tissues are obtained by balanced SSFP compared to other SSFP sequences as seen from Figure 2.2 provided in [1].

In fully balanced SSFP, the most significant part is refocusing of all three gradient axes, which follows that gradient integrals in all axes should be zero in

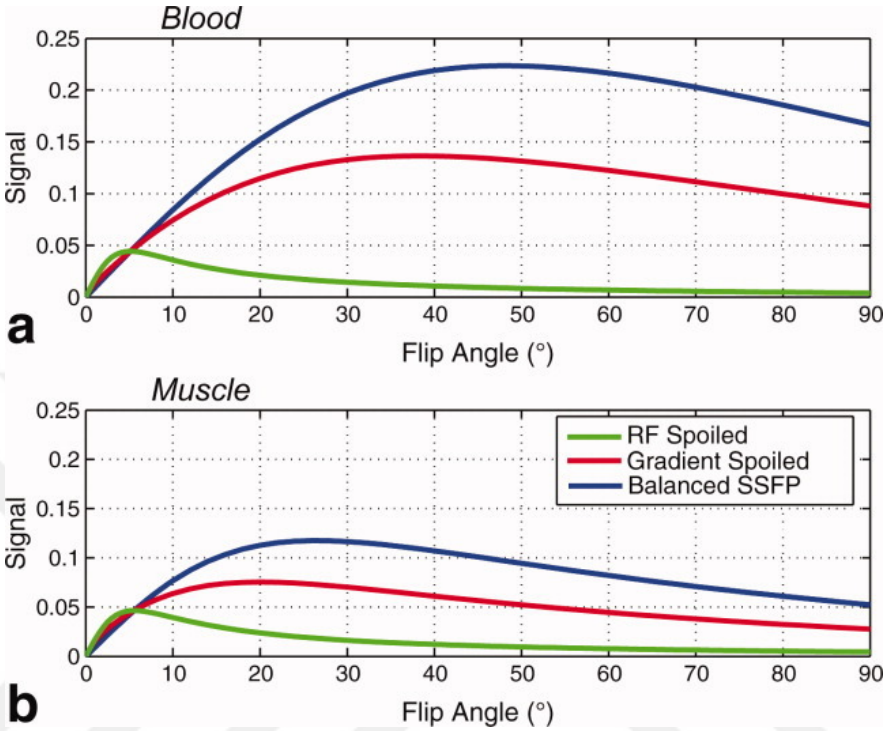

Figure 2.2: Signal amplitudes of RF-spoiled, Gradient spoiled and balanced SSFP sequences obtained over varying flip angles for blood and muscle.

one TR interval. In this way, only one signal magnetization vector remains at the end of a TR as demonstrated in Figure 2.3 provided in Ref.[2] by visualization of evolution of the magnetization, and also balanced gradients in bSSFP sequence.

2.2.1 Signal Equation Derivation for bSSFP

Here, we provide derivation of the bSSFP signal equation according to movements of magnetization vector within and between TR intervals. We denote the magnetization vector just before the RF pulse with a minus sign over magnetization vector $\bar{M}$ ($\bar{M}^-$) and just after the RF pulse with a plus sign over magnetization vector $\bar{M}$ ($\bar{M}^+$), flip angle with α, phase shift due to off-resonance with θ, rotation matrices with $R_{\{x,y,z\}}$, equilibrium magnetization with M_0, and exponents of relaxation parameters T_1 and T_2 as a function of time with $E_1(t) = exp(-t/T_1)$ and $E_2(t) = exp(-t/T_2)$ respectively.

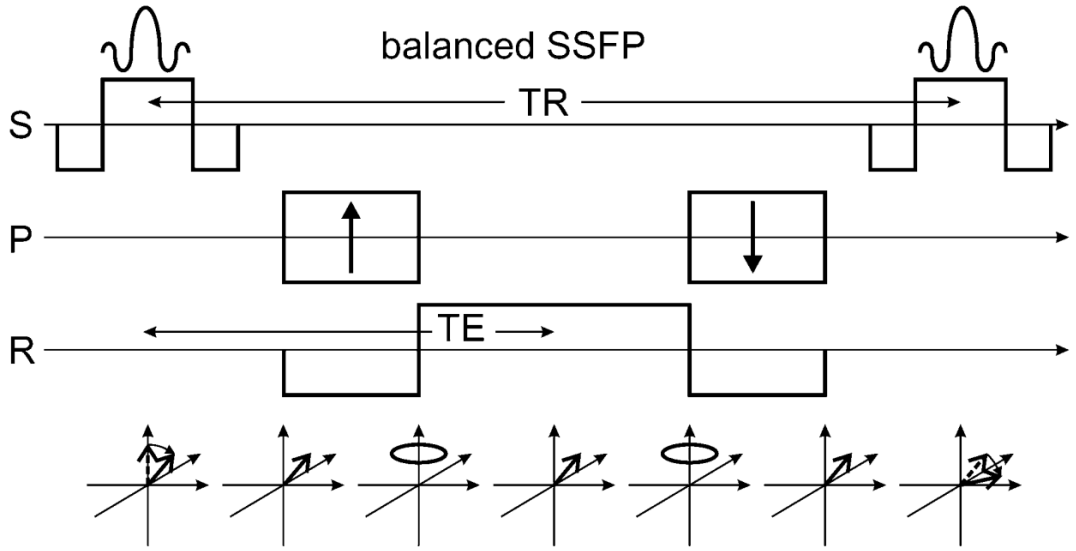

Figure 2.3: Visualisation of the magnetization evolution and balanced gradients in bSSFP sequence

1. RF pulse applied at the beginning of a TR interval leads to rotation of the magnetization vector ($\bar{M}^-$) about an arbitrary axis in transverse plane (we can assume its rotation is about x-axis):

$$\bar{M}^+ = R_x(\alpha)\bar{M}^- \tag{2.7}$$

2. At the end of one TR, off-resonance causes rotation of magnetization vector $\bar{M}^+$ about z-axis by θ degree in total. Then this rotation is followed by relaxation of transverse and longitudinal magnetization. In the mean time, magnetization M_0 starts to reappear in longitudinal z direction. So the magnetization vector just before the next RF pulse $\bar{M}^-$ (assuming that steady state is reached) can be written as summation of these movements as in following:

$$\bar{M}^- = E(t = TR)R_z(\theta)\bar{M}^+ + (1 - E_1(t = TR))\bar{M}_0 \tag{2.8}$$

$$\text{where } \bar{M}_0 = [0, 0, M_0]^T \tag{2.9}$$

$$\text{and } E(t) = \text{diag}\{E_2(t), E_2(t), E_1(t)\} \tag{2.10}$$

3. Then, an RF pulse is applied after previous TR interval, which leads to rotation around x-axis again. By considering that the steady state is reached, magnetization vector just after the RF pulse can be written by multiplying the $\bar{M}^-$ in Equation 2.8 from left with the rotation matrix R_x:

$$\bar{M}^+ = R_x(\alpha)E(t = TR)R_z(\theta)\bar{M}^+ + R_x(\alpha)(1 - E_1(t = TR))\bar{M}_0 \tag{2.11}$$

$$\bar{M}^+ = (I - R_x(\alpha)E(t = TR)R_z(\theta))^{-1}R_x(\alpha)(1 - E_1(t = TR))\bar{M}_0 \tag{2.12}$$

After the statement inside inverse term is derived and placed into its place:

$$\bar{M}^+ = \begin{bmatrix} 1 - E_2\cos\theta & -E_2\sin\theta & 0 \\ E_2\sin\theta\cos\alpha & 1 - E_2\cos\theta\cos\alpha & -E_1\sin\theta \\ -E_2\sin\theta\sin\alpha & E_2\cos\theta\sin\alpha & 1 - E_1\cos\alpha \end{bmatrix}^{-1} \begin{bmatrix} 0 \\ \sin\alpha \\ \cos\alpha \end{bmatrix} (1 - E_1)M_0 \tag{2.13}$$

If we denote the derived matrix as Q, its inverse can be found with:

$$Q^{-1} = \frac{\text{adj}(Q)}{\det(Q)} \tag{2.14}$$

where

$$\text{adj}(Q) = \begin{bmatrix} K_1 & -E_2\sin\theta(1 - E_1\cos\alpha) & E_1E_2\sin\theta\sin\alpha \\ K_2 & (1 - E_2\cos\theta)(1 - E_1\cos\alpha) & E_1(1 - E_2\cos\theta)\sin\alpha \\ K_3 & K_4 & K_5 \end{bmatrix} \tag{2.15}$$

and

$$\det(Q) = (1 - E_1\cos\alpha)(1 - E_2\cos\theta) - E_2(E_1 - \cos\alpha)(E_2 - \cos\theta) \tag{2.16}$$

. Here, we denote matrix entries which do not have any contribution while

calculating the transverse magnetization with K_i's for simplicity. If everything is placed into their places in Equation 2.13:

$$\bar{M}^+ = \frac{(1-E_1)M_0}{(1-E_1\cos\alpha)(1-E_2\cos\theta)-E_2(E_1-\cos\alpha)(E_2-\cos\theta)} \begin{bmatrix} E_2\sin\theta\sin\alpha \\ (1-E_2\cos\theta)\sin\alpha \\ K_6 \end{bmatrix} \tag{2.17}$$

Then, transverse magnetization vector's components on x-axis M_x and y-axis M_y can be written as:

$$M_x^+ = \frac{M_0(1-E_1)E_2\sin\theta\sin\alpha}{(1-E_1\cos\alpha)(1-E_2\cos\theta)-E_2(E_1-\cos\alpha)(E_2-\cos\theta)} \tag{2.18}$$

$$M_y^+ = \frac{M_0(1-E_1)(1-E_2\cos\theta)\sin\alpha}{(1-E_1\cos\alpha)(1-E_2\cos\theta)-E_2(E_1-\cos\alpha)(E_2-\cos\theta)} \tag{2.19}$$

If a vector in the transverse plane is defined with a complex plane where x and y axes correspond to real and imaginary axes respectively, the net transverse magnetization just after the RF pulse can be expressed as:

$$M_{xy}^+ = M_x^+ + iM_y^+ = \frac{iM_0(1-E_1)\sin\alpha(1-E_2e^{i\theta})}{(1-E_1\cos\alpha)(1-E_2\cos\theta)-E_2(E_1-\cos\alpha)(E_2-\cos\theta)} \tag{2.20}$$

where $E_1 = \exp(-TR/T_1)$ and $E_2 = \exp(-TR/T_2)$.

4. Then the net magnetization of the signal acquired at TE becomes:

$$M_{xy}(TE) = M_{xy}^+ e^{-TE/T_2} e^{i\theta TE/TR} \tag{2.21}$$

In summary, the bSSFP signal acquired at TE with flip angle α is expressed as:

$$M_{xy}(TE) = \frac{iM_0(1-E_1)\sin\alpha(1-E_2e^{i\theta})e^{-TE/T_2}e^{i\theta TE/TR}}{(1-E_1\cos\alpha)(1-E_2\cos\theta)-E_2(E_1-\cos\alpha)(E_2-\cos\theta)} \tag{2.22}$$

2.2.2 Phase Cycled Balanced SSFP

Although bSSFP is a rapid imaging sequence providing high SNR, its sensitivity to field inhomogeneity is the main drawback of the sequence, therefore it is highly affected by the change in the phase due to off-resonance frequencies. This is because, signal losses called banding artifacts are seen in some spatial locations of the produced image. Figure 2.4 demonstrates an example in vivo image where banding artifacts are observed in the image as a dark band passing through the middle of the image. Locations of these artifacts can be shifted spatially by changing the phase increments of the RF pulse, by changing the repetition time, or by shimming.

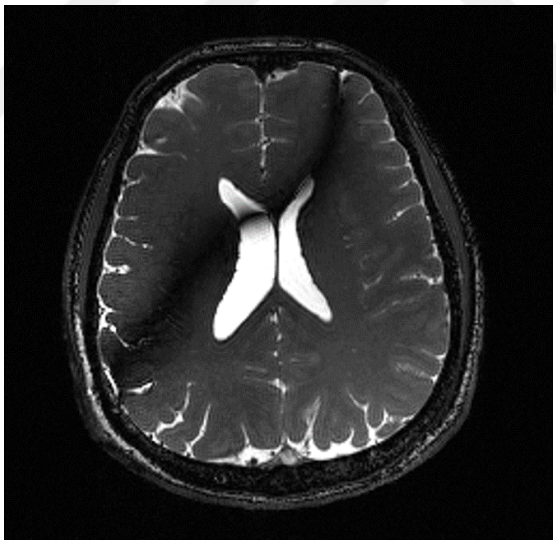

Figure 2.4: An example in vivo bSSFP image where banding artifact is observed as a dark band passing through the middle of the image.

The procedure where the phase of the RF pulse is alternated is called phase-cycling. If phase of the RF pulse is incremented at each TR in bSSFP imaging, it is called phase-cycled balanced SSFP. Phase-cycled bSSFP is generally used to remove the banding artifacts [3] by acquiring multiple phase-cycled bSSFP data with different phase increments such that locations of the banding artifacts are different in each acquisition. Figure 2.5 demonstrates an example of multiple-acquisition phase-cycled bSSFP in vivo images obtained with 0, $\pi/2$, π and $3\pi/2$ RF phase increments respectively from left to right. Then, these acquisitions can

be combined with various methods to get the banding-free image.

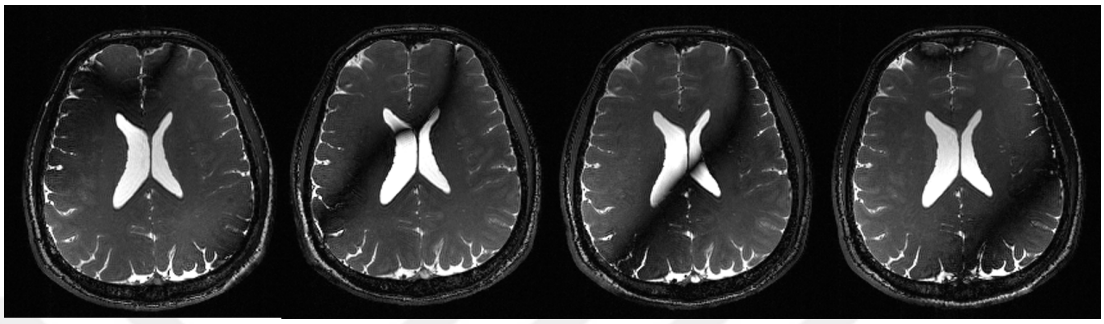

Figure 2.5: Example in vivo multiple-acquisition phase cycled bSFFP images acquired with 0, $\pi/2$, π and $3\pi/2$ RF phase increments are shown from left to right respectively.

The reason why dark bands occur in some locations of the image can be understood by observing the signal evolution over the phase. Figure 2.6 shows the phase-cycled bSSFP signal profile for different phase increments. As seen from the figure that the bSSFP signal profile has a region where signal intensity is high which is called pass-band, and a region where signal intensity is really low which is called stop-band. Therefore, we can interpret banding artifacts as lower signal intensities at stop-band. Furthermore, we can see that the profile is shifted along the phase offset direction as phase increments are changed. We can also observe that different signal intensities of the same sample are captured by multiple phase-cycled acquisitions. And this is because why multiple-acquisition phase-cycling helps to eliminate artifacts.

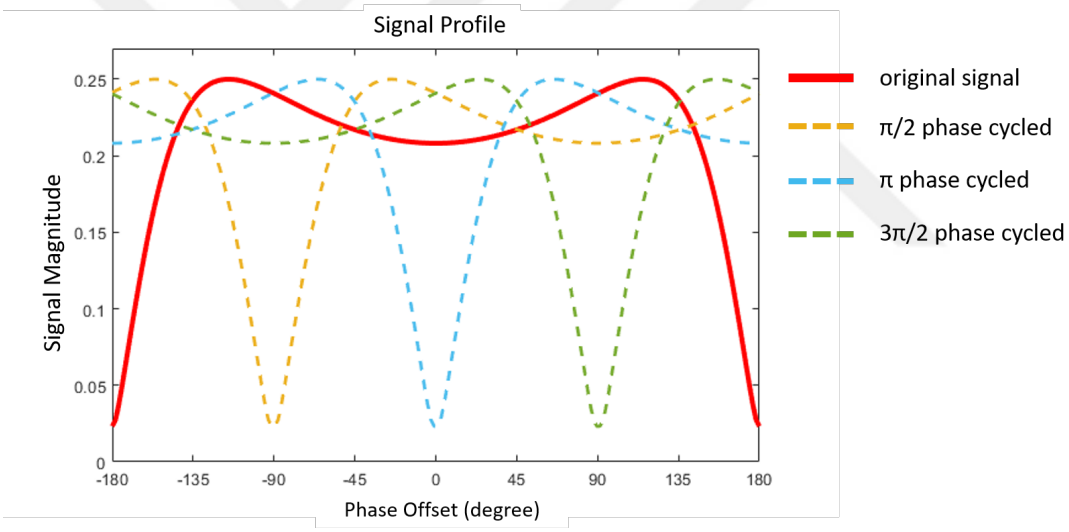

Figure 2.6: Phase-cycled bSSFP signal profile over phase-offset for four different RF phase increments. The bSSFP signal with 0, $\pi/2$, π and $3\pi/2$ phase increments are shown with red, yellow, blue and green lines respectively.

Chapter 3

Efficient Parameter Mapping for MRI with Phase-cycled bSSFP

3.1 Introduction

Balanced steady-state free precession (bSSFP) is an MRI sequence that offers very high signal-to-noise ratios (SNR) in short scan times [4]. Yet this efficiency comes at the expense of distinct signal characteristics compared to conventional sequences. A main difference is the sensitivity of the bSSFP signal to main field inhomogeneities, which causes banding artifacts near regions of large off-resonance shifts [2]. While a number of approaches were proposed to mitigate artifacts [5, 6, 7, 8, 9], arguably the most common method is phase-cycled bSSFP imaging [10]. Multiple acquisitions of the same anatomy are first collected for a range of different RF phase-cycling increments. A signal combination across phase cycles then reduces severity of artifacts [10, 11, 12, 13]. Intensity-based combinations assume that banding artifacts are spatially non-overlapping across phase cycles, and that for each voxel there is at least one phase cycle with high signal intensity. In practice, intensity-based methods can perform suboptimally for certain ranges of relaxation parameters or flip angles [10]. For improved artifact suppression,

recent studies have proposed model-based approaches to estimate the banding-free component of the bSSFP signal. To do this, Linearization for Off-Resonance Estimation-Gauss Newton (LORE-GN) uses a linearized model of the nonlinear bSSFP signal [14]; Elliptical Signal Model (ESM) employs an elliptical model for the complex bSSFP signal [15, 16]; and dictionary-based methods such as trueCISS simulate the bSSFP signal for various tissue/imaging parameters and then perform identification via comparisons against actual measurements [17]. These model-based techniques can perform reliably across practical ranges of tissue and sequence parameters.

An equally important difference of bSSFP is its nonstandard T_2/T_1-dependent contrast [1, 18], which can be considered an advantage for applications focusing on bright fluid signals such as cardiac imaging and angiography [19, 20, 21, 22]. That said, bSSFP might yield suboptimal contrast for other applications that focus on primarily T_2- or T_1-driven differences among soft tissues. A powerful approach to address this limitation is to estimate relaxation parameters from bSSFP acquisitions, and to either directly examine the estimates [23] or synthesize images of desired contrasts [24]. Many previous methods in this domain rely on introduction of additional T_1- or T_2-weighting information into measurements. Given prior knowledge of T_1 values, Driven-equilibrium single pulse observation of T_2 (DESPOT2) estimates T_2 values from N=2-4 acquisitions using a linearized signal equation [25, 26]. Yet, T_1 values are typically estimated via two SPGR acquisitions at different flip angles that are not as scan efficient as bSSFP. An alternative is to use magnetization-preparation modules in conjunction with bSSFP to enable T_1 estimation [27] or simulatenous T_1 and T_2 estimation [28, 29]. Magnetization-preparation modules reduce scan efficiency, and these methods can be susceptible to field inhomogeneity when based on a single phase-cycled acquisition. Dictionary-based methods for parameter estimation have also been combined with bSSFP sequences with varying parameters across readouts as in Magnetic Resonance Fingerprinting [30]. While dictionary-based methods enable estimation of many tissue and imaging parameters including T_1 and T_2, they require advanced pulse sequence designs that may not be available at all sites.

As an alternative, recent studies have proposed parameter mapping based on standard phase-cycled bSSFP. The trueCISS method uses N=16 acquisitions to compare the measured signal profile across phase cycles against a simulated dictionary of signal profiles [17]. While trueCISS can estimate the equilibrium magnetization, the T_1/T_2 ratio and off-resonance, it does not consider explicit estimation of T_1 or T_2. LORE-GN instead performs least-squares estimation of T_1 and T_2 based on linearized equations [14]. That said, accurate T_1 and T_2 estimation was suggested to be difficult with N=4 at practical SNR levels. Recently, the PLANET method based on ESM was proposed to demonstrate feasability of simultaneous T_1 and T_2 estimation [31]. PLANET first fits an ellipse to multiple-acquisition bSSFP measurements, and then analytically estimates T_1 and T_2 values for each voxel by observing geometric properties [31]. Theoretical treatment suggested that N$\geq$6 is required for ellipse fitting; and demonstrations were performed at N=10 to improve noise resilience [31, 32]. Despite the elegance of this recent approach, the use of relatively large N partly limits scan efficiency.

Here, we propose a new method based on the ESM framework, CELF, for parameter estimation with fewer number of bSSFP acquisitions. To improve efficiency, CELF introduces additional geometric constraints to ellipse fitting, such that the number of unknowns and the required number of acquisitions can be reduced to N=4. The central line of the ellipse is identified via a geometric solution [15], and then incorporated as prior knowledge for a constrained ellipse fit. To improve accuracy, a dictionary-based identification is leveraged to obtain a final ellipse fit. T_1, T_2, off-resonance, and on-resonant signal intensity values are analytically derived from the geometric properties of the ellipse. Comprehensive evaluations are performed via simulations as well as phantom and in vivo experiments. These evaluations clearly indicate that CELF enables improved accuracy and efficiency in parameter estimation compared to direct ellipse fitting.

3.2 Theory

The main aim of this study is to develop an improved method for parameter estimation from multiple-acquisition phase-cycled bSSFP measurements. The proposed method is based on the elliptical signal model for complex phase-cycled bSSFP signals. It fits an ellipse in each voxel to estimate the equilibrium magnetization, off-resonance, and T_1 and T_2 values. To enable parameter estimation with fewer number of acquisitions, additional geometric constraints are incorporated into the ellipse fitting problem. To improve estimation accuracy, a dictionary-based ellipse identification procedure is used. In the following subsections, we overview fundamentals of the elliptical signal model and the direct ellipse fitting formulation. We then describe the proposed constrained ellipse fitting formulation, and discuss the novel contributions of our work.

3.2.1 Elliptical Signal Model for Phase-cycled bSSFP

Analytical expression of the bSSFP signal

The steady-state signal generated by a phase-cycled bSSFP sequence right after the radio-frequency (RF) excitation can be expressed as [15]:

$$S_{base} = M\frac{1 - ae^{i\theta}}{1 - b\cos\theta} \tag{3.1}$$

where

$$\begin{aligned} a &= E_2 \\ b &= \tfrac{E_2(1-E_1)(1+\cos\alpha)}{1-E_1\cos\alpha-E_2^2(E_1-\cos\alpha)} \\ M &= \tfrac{M_0(1-E_1)\sin\alpha}{1-E_1\cos\alpha-E_2^2(E_1-\cos\alpha)} \end{aligned} \tag{3.2}$$

In Eq. 3.2, $E_1 = exp(-TR/T_1)$ and $E_2 = exp(-TR/T_2)$ define time constants of exponential decay for longitudinal and transverse magnetization, namely T_1 and T_2 relaxation times. TR denotes the repetition time, M_0 is the equilibrium magnetization, and α is the flip angle of the RF excitation. Meanwhile, $\theta =$

$\theta_0 - \Delta\theta$, where $\theta_0 = 2\pi(\Delta f_0 + \delta_{cs})$TR reflects phase accrual due to main field inhomogeneity at off-resonance frequency Δf_0 and chemical shift frequency δ_{cs}, and $\Delta\theta$ reflects phase accrual due to RF phase-cycling. In multiple-acquisition bSSFP, N separate measurements are obtained while the $\Delta\theta$ is spanned across $[0, 2\pi)$ in equispaced intervals (e.g. $\Delta\theta = \{0, \pi/2, \pi, 3\pi/2\}$ for N=4).

For measurements performed at the echo time TE, the base signal expressed in Eq. 3.1 gets scaled and rotated as follows:

$$S = KMe^{-TE/T_2}\frac{1 - ae^{i\theta}}{1 - b\cos\theta}e^{i\phi} \tag{3.3}$$

where K is a complex scalar denoting coil sensitivity, $\phi = 2\pi(\Delta f_0 + \delta_{cs})TE + \phi_{total}$ represents the aggregate phase accrual, and ϕ_{total} captures phase accumulation due to system imperfections including eddy currents and main field drifts.

The unknown tissue-dependent parameters to be estimated in the measured bSSFP signal are T_1, T_2, M_0 and Δf_0. Meanwhile, the values of user-controlled imaging parameters TR, TE, α and $\Delta\theta$ are assumed to be known. Thus, M, a, b and θ that parametrize the bSSFP signal in Eq. 3.3 depend on both known and unknown parameters via nonlinear relations.

Elliptical Signal Model

A powerful framework to examine the link between the signal parameters and the actual measurements is the elliptical signal model (ESM) by Xiang and Hoff [15]. The ESM framework observes that for a given voxel Eq. 3.1 describes an ellipse in the complex plane for bSSFP signals. Each bSSFP measurement acquired with a specific phase-cycling increment ($\Delta\theta$) projects onto a point on this ellipse, as demonstrated in Fig. 3.1a. Characteristic properties of the bSSFP ellipse in terms of the parameters in Eq. 3.2 are defined below [15]:

- Semi-major, semi-minor axes: $M\frac{a}{\sqrt{1-b^2}}$ and $M\frac{|a-b|}{1-b^2}$ (3.4)
- Geometric center: $(M\frac{1-ab}{1-b^2}, 0)$ (3.5)

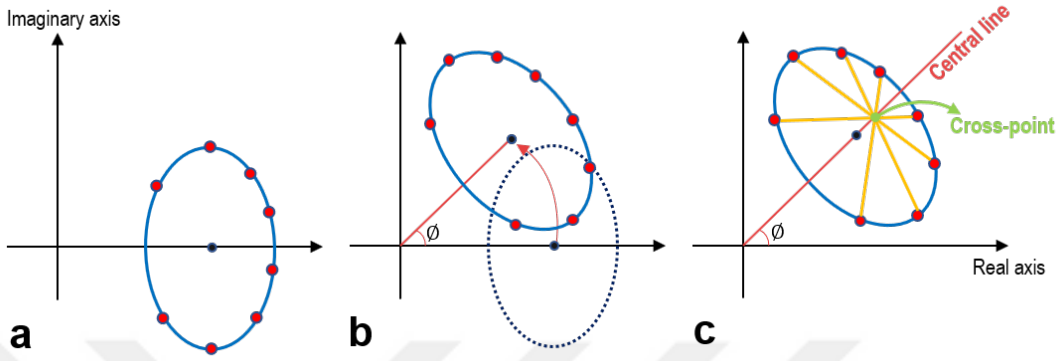

Figure 3.1: (a) The complex-valued base bSSFP signal S_{base} following the RF excitation defines a vertically-oriented ellipse. The signal values at different phase-cycling increments $\Delta\theta$ project onto separate points on this ellipse (shown with red dots). (b) The measured bSSFP signal at echo time (TE) constitutes a scaled and rotated version of the ellipse for S_{base}. (c) The ellipse cross-point is at the intersection of line segments that connect measurement pairs: (i, j) is a pair if $|\Delta\theta_i - \Delta\theta_j| = \pi$. The central line of the ellipse passes through both the ellipse center and cross-point.

- Eccentricity: $\sqrt{1 - \frac{(a-b)^2}{a^2(1-b^2)}}$ (3.6)
- Condition for vertically-oriented ellipse: $b < \frac{2a}{1+a^2}$ (3.7)

Note that ESM offers ease of geometric interpretation for the bSSFP signal. For instance, the ellipse for the measured bSSFP signals in Eq. 3.3 can easily be observed to be a scaled and rotated version of the ellipse of the base signals in Eq. 3.1, as illustrated in Fig. 3.1b.

Geometric Solution

A common method to estimate an on-resonant bSSFP image via ESM involves identifying the geometric solution (GS) of the ellipse [15]. Measurements are paired based on the difference between their phase-cycling increments such that (i, j) is a pair if $|\Delta\theta_i - \Delta\theta_j| = \pi$. GS is defined as the cross-point of all formulated pairs. For example, the pairs for N=4 are: (1,3) with $|0 - \pi| = \pi$; (2,4) with $|\frac{\pi}{2} - \frac{3\pi}{2}| = \pi$. Note that GS of the ellipse in Eq. 3.1 corresponds to the parameter

M in Eq. 3.2, and GS of the ellipse in Eq. 3.3 is a scaled and rotated version of M. Since M does not depend on θ, it can be used to produce an on-resonant bSSFP image that does not suffer from banding artifacts [15].

Here we aim to work with an arbitrary number of bSSFP acquisitions. The original GS can be extended to N acquisitions via the following system of equations:

$$\begin{bmatrix} y_{m+1} - y_1 & x_1 - x_{m+1} \\ y_{m+2} - y_2 & x_2 - x_{m+2} \\ \vdots & \vdots \\ y_N - y_m & x_m - x_N \end{bmatrix} \begin{bmatrix} x_0 \\ y_0 \end{bmatrix} = \begin{bmatrix} x_1 y_{m+1} - x_{m+1} y_1 \\ x_2 y_{m+2} - x_{m+2} y_2 \\ \vdots \\ x_m y_N - x_N y_m \end{bmatrix} \tag{3.8}$$

where $(x, y)_i$ denote the real and imaginary components of S in the i^{th} acquisition, $(x, y)_i$ and $(x, y)_{m+i}$ form a π-separated signal pair ($m = N/2$ and $i = 1, 2, .., m$), and $q = (x_0, y_0)$ is the cross-point of the ellipse. The cross-point can be estimated by ordinary least-squares estimation.

3.2.2 Direct Ellipse Fitting

The unknown parameters (T_1, T_2, M_0, Δf_0) can be estimated by fitting an ellipse to the collection of N phase-cycled bSSFP signals for a given voxel. To do this, the PLANET method uses Fitzgibbon's direct least square fitting of ellipses [33]. In quadratic polynomial form, an ellipse can be described as:

$$f(\boldsymbol{x}) = \nu_1 x^2 + \nu_2 xy + \nu_3 y^2 + \nu_4 x + \nu_5 y + \nu_6 = 0 \tag{3.9}$$

where $\boldsymbol{\nu} = \begin{bmatrix} \nu_1 & \nu_2 & \nu_3 & \nu_4 & \nu_5 & \nu_6 \end{bmatrix}^T$ is the polynomial coefficient vector, and $\boldsymbol{x} = \begin{bmatrix} x & y \end{bmatrix}^T$ is a point on the ellipse where x and y denote the real and imaginary components S, respectively. Taking the cost function to be the algebraic

distance between measured data points and the fit ellipse, the following least-sqaures formulation can be obtained:

$$\left\| \begin{bmatrix} f(\boldsymbol{x}_1) \\ \vdots \\ f(\boldsymbol{x}_N) \end{bmatrix} \right\|_2^2 = \left\| \begin{bmatrix} x_1^2 & x_1 y_1 & y_1^2 & x_1 & y_1 & 1 \\ \vdots & \vdots & \vdots & \vdots & \vdots & \vdots \\ x_N^2 & x_N y_N & y_N^2 & x_N & y_N & 1 \end{bmatrix} \begin{bmatrix} \nu_1 \\ \nu_2 \\ \nu_3 \\ \nu_4 \\ \nu_5 \\ \nu_6 \end{bmatrix} \right\|_2^2 = \|D\boldsymbol{\nu}\|_2^2 \tag{3.10}$$

where $f(\boldsymbol{x}_i)$ denotes the value of the polynomial function evaluated at the i^{th} data point $\boldsymbol{x}_i$, and D is the agreegate data matrix for N acquisitions. The minimization of sum of squared errors $\sum_{i=1}^{N} |f(\boldsymbol{x}_i)|^2$ can be cast as an optimization problem:

$$\begin{aligned} \underset{\boldsymbol{\nu}}{\text{minimize}} \quad & \|D\boldsymbol{\nu}\|_2^2 \\ \text{subject to} \quad & \boldsymbol{\nu}^T C \boldsymbol{\nu} = 1 \end{aligned} \tag{3.11}$$

where $C = \left[\begin{array}{ccc:c} 0 & 0 & 2 & \\ 0 & -1 & 0 & 0_{3\times3} \\ 2 & 0 & 0 & \\ \hdashline & 0_{3\times3} & & 0_{3\times3} \end{array}\right]$ is the constraint matrix ensuring that the fit polynomial is an ellipse. An analytical solution can be obtained by solving an equivalent generalized eigenvalue problem (GEP):

$$D^T D\boldsymbol{\nu} = \lambda C\boldsymbol{\nu} \tag{3.12}$$

In sum, Fitzgibbon's method solves Eq. 3.12 to obtain the best fit ellipse. This method constrains the solution to an ellipse, it is non-iterative and numerically stable [34]. Note that the quadratic form of an ellipse is uniquely specified by six scalar coefficients in $\boldsymbol{\nu}$, so a theoretical minimum of N=6 is needed for fitting. Yet MRI acquisitions are inherently noisy, and this can reduce accuracy of ellipse fits particularly for relatively lower N. To mitigate this problem, previous studies

have used up to N=10 at the expense of prolonged scan times [31, 32].

3.2.3 Constrained Ellipse Fitting

To improve scan efficiency, here we propose a new method that enables ellipse fits and improves their accuracy with relatively low N. The proposed constrained ellipse fitting method (CELF) incorporates geometric prior knowledge about the ellipse center to enable unique specification of the ellipse based on solely four data points [35]. To further improve quality of ellipse fits, CELF then employs a dictionary-based ellipse identification procedure. Parameter estimation is finally performed on the identified ellipses. These individual components of CELF are described in detail below.

Formulation of CELF

To facilitate integration of the geometric prior in the fitting procedure, here we use a centralized quadratic function to describe the ellipse:

$$f(\boldsymbol{x}) = (\boldsymbol{x} - \boldsymbol{x_c})^T A(\boldsymbol{x} - \boldsymbol{x_c}) + g = 0 \tag{3.13}$$

where $A = \begin{bmatrix} c_1 & \frac{c_2}{2} \\ \frac{c_2}{2} & c_3 \end{bmatrix}$ is a positive definite matrix describing the orientation and eccentricity of the ellipse, $\boldsymbol{x} = \begin{bmatrix} x & y \end{bmatrix}^T$ is a point on the ellipse, $\boldsymbol{x_c} = \begin{bmatrix} x_c & y_c \end{bmatrix}^T$ is the center of the ellipse, and g is a finite negative scalar determining the area of the ellipse. The scalar form of Eq. 3.13 is given as:

$$c_1(x - x_c)^2 + c_2(x - x_c)(y - y_c) + c_3(y - y_c)^2 + g = 0 \tag{3.14}$$

Note that Eq. 3.14 still contains six unknowns: c_1, c_2, c_3, g along with x_c and y_c.

CELF uses prior knowledge on the ellipse's central line for improved ellipse fitting at lower N. To leverage this prior, we first observe that the base bSSFP

signal S_{base} in Eq. 3.1 forms a vertically-oriented ellipse, with the semi-major axis perpendicular to the line passing through its center and the origin. Meanwhile, the measured bSSFP signal S in Eq. 3.3 can be obtained by rotating the base ellipse at an arbitrary angle. Therefore, the ellipse for S can be back-rotated around the origin to produce the base version. This back-rotation will place the central line of the ellipse along the x-axis. The orientation-eccentricity matrix will then be diagonal ($c_2 = 0$; $\tilde{A} = \begin{bmatrix} c_1 & 0 \\ 0 & c_3 \end{bmatrix}$), the center $\tilde{\boldsymbol{x}}_{\boldsymbol{c}}$ will only have a real component.

Next, we express the ellipse center as a scaled version of the cross-point q, which is given by the geometric solution. In particular, $\tilde{\boldsymbol{x}}_{\boldsymbol{c}} = \begin{bmatrix} x_c & y_c \end{bmatrix} = \begin{bmatrix} \gamma q & 0 \end{bmatrix}^T$, where γ is an unknown scaling parameter. With a transformation of the coordinate system, the spatial coordinates of the data points in the back-rotated ellipse can be described as $\tilde{\boldsymbol{x}} = \begin{bmatrix} \tilde{x} & \tilde{y} \end{bmatrix}^T$. The ellipse equation in Eq. 3.13 then becomes:

$$\begin{aligned} f(\tilde{\boldsymbol{x}}) &= \begin{bmatrix} \tilde{x} - \gamma q & \tilde{y} \end{bmatrix} \begin{bmatrix} c_1 & 0 \\ 0 & c_3 \end{bmatrix} \begin{bmatrix} \tilde{x} - \gamma q \\ \tilde{y} \end{bmatrix} + g \\ &= \begin{bmatrix} \tilde{x} & \tilde{y} \end{bmatrix} \begin{bmatrix} c_1 & 0 \\ 0 & c_3 \end{bmatrix} \begin{bmatrix} \tilde{x} \\ \tilde{y} \end{bmatrix} - 2\gamma \begin{bmatrix} q & 0 \end{bmatrix} \begin{bmatrix} c_1 & 0 \\ 0 & c_3 \end{bmatrix} \begin{bmatrix} \tilde{x} \\ \tilde{y} \end{bmatrix} + g + c_1\gamma^2 q^2 \\ &= c_1\tilde{x}^2 + c_3\tilde{y}^2 - 2\gamma c_1 q\tilde{x} + h \end{aligned} \tag{3.15}$$

where $h = g + c_1\gamma^2 q^2$ is a scalar. In this formulation, the set of unknowns is reduced to c_1, c_3, γ, and h. Thus, N=4 acquisitions are sufficient for ellipse fitting in principle.

Similar to direct ellipse fitting, the error measure of algebraic distance between

measured data points and the fit ellipse leads to a least-squares problem:

$$\begin{aligned}\left\|\begin{bmatrix} f(\tilde{\boldsymbol{x}}_1) \\ \vdots \\ f(\tilde{\boldsymbol{x}}_N) \end{bmatrix}\right\|_2^2 &= \left\|\left(\begin{bmatrix} \tilde{\boldsymbol{x}}_1^2 & \tilde{\boldsymbol{y}}_1^2 & 1 \\ \vdots & \vdots & \vdots \\ \tilde{\boldsymbol{x}}_N^2 & \tilde{\boldsymbol{y}}_N^2 & 1 \end{bmatrix} - \gamma \begin{bmatrix} 2q\tilde{\boldsymbol{x}}_1 & 0 & 0 \\ \vdots & \vdots & \vdots \\ 2q\tilde{\boldsymbol{x}}_N & 0 & 0 \end{bmatrix}\right) \begin{bmatrix} c_1 \\ c_3 \\ h \end{bmatrix}\right\|_2^2 \\ &= \left\|\left(\begin{bmatrix} D_0 & \mathbf{1}_N \end{bmatrix} - \gamma \begin{bmatrix} D_1 & \mathbf{0}_N \end{bmatrix}\right) \begin{bmatrix} \boldsymbol{u} \\ h \end{bmatrix}\right\|_2^2 \\ &= Q(\gamma, \boldsymbol{u}, h)\end{aligned} \tag{3.16}$$

where $f(\tilde{\boldsymbol{x}}_i)$ denotes the value of the polynomial function evaluated at the i^{th} back-rotated data point $\tilde{\boldsymbol{x}}_i$, D_0 and D_1 are aggregate data matrices for N acquisitions, $\boldsymbol{u} = \begin{bmatrix} c_1 & c_3 \end{bmatrix}^T$ is defined as a parameter vector for $\tilde{A}$. The cost function is taken as $Q = \sum_{i=1}^{N} |f(\tilde{\boldsymbol{x}}_i)|^2$.

To constrain the solution of Eq. 3.16 to a strict ellipse, A must be positive definite, i.e., all leading principal minors of A are positive: $\det\left(\begin{bmatrix} c_1 \end{bmatrix}\right) = c_1 > 0$ and $\det(A) = (4c_1c_3 - c_2^2)/4 > 0$. To introduce rotation/translation invariance and to reduce the degrees of freedom, $\det(A)$ is set to a constant positive number without loss of generality [33]. In this case, constraining the fit to an ellipse is equivalent to the following conditions [35]: $4\det(A) = 4c_1c_3 - c_2^2 = 1$ and $c_1 > 0$. Since $c_2 = 0$ in the back-rotated form $\tilde{A}$, these conditions simply to$4c_1c_3 = 1$ and $c_1 > 0$. These two conditions are integrated to the ellipse fitting procedure as additional constraints:

$$\begin{aligned}\boldsymbol{u}^T B \boldsymbol{u} &= \begin{bmatrix} c_1 & c_3 \end{bmatrix} \begin{bmatrix} 0 & 2 \\ 2 & 0 \end{bmatrix} \begin{bmatrix} c_1 \\ c_3 \end{bmatrix} = 1, \\ \boldsymbol{u}^T \boldsymbol{d} &= \begin{bmatrix} c_1 & c_3 \end{bmatrix} \begin{bmatrix} 1 \\ 0 \end{bmatrix} > 0\end{aligned} \tag{3.17}$$

where B is the constraint matrix and $\boldsymbol{d}$ is the constraint vector.

Lastly, defining the cost function in terms of the unknown parameters γ, $\boldsymbol{u}$

and h, the constrained ellipse fitting problem can be stated as follows:

$$\begin{aligned} \underset{\gamma,\boldsymbol{u},h}{\text{minimize}} \quad & Q(\gamma,\boldsymbol{u},h) \\ \text{subject to} \quad & \boldsymbol{u}^T B\boldsymbol{u} = 1, \text{ and } \boldsymbol{u}^T\boldsymbol{d} > 0 \end{aligned} \tag{3.18}$$

Solution of CELF

It is challenging to obtain a single-shot solution to Eq. 3.18 that estimates all unknowns simultaneously as in direct ellipse fitting. Here we instead use a progressive approach to sequentially identify the unkown parameters [35]:

$$\begin{aligned} \min_{\substack{\gamma,\boldsymbol{u},h \\ \boldsymbol{u}^T B\boldsymbol{u}=1 \\ \boldsymbol{u}^T\boldsymbol{d}>0}} Q(\gamma,\boldsymbol{u},h) &= \min_{\gamma} \quad \min_{\substack{\boldsymbol{u} \\ \boldsymbol{u}^T B\boldsymbol{u}=1 \\ \boldsymbol{u}^T\boldsymbol{d}>0}} \quad \min_{h} Q(\gamma,\boldsymbol{u},h) \\ &= \min_{\gamma} \quad \min_{\substack{\boldsymbol{u} \\ \boldsymbol{u}^T B\boldsymbol{u}=1 \\ \boldsymbol{u}^T\boldsymbol{d}>0}} \quad Q_2(\gamma,\boldsymbol{u}) \\ &= \min_{\gamma} \quad Q_3(\gamma) \end{aligned} \tag{3.19}$$

where the minimization is decomposed into three subproblems to estimate h, $\boldsymbol{u}$, and γ, respectively.

Subproblem 1. The first subproblem is defined as a minimization over the parameter h, and it aims to optimize h conditioned on the values of the remaining parameters $(\gamma, \boldsymbol{u})$ as follows:

$$\min_{h} Q_1(\gamma,\boldsymbol{u},h) \tag{3.20}$$

and it is equivalent to:

$$\begin{aligned}
&\min_h \left\| \left(\begin{bmatrix} D_0 & \mathbf{1}_N \end{bmatrix} - \gamma \begin{bmatrix} D_1 & \mathbf{0}_N \end{bmatrix} \right) \begin{bmatrix} \boldsymbol{u} \\ h \end{bmatrix} \right\|_2^2 \\
&\equiv \min_h \ ((D_0 - \gamma D_1)\boldsymbol{u} + \mathbf{1}_N h)^T ((D_0 - \gamma D_1)\boldsymbol{u} + \mathbf{1}_N h) \\
&\equiv \min_h \ \boldsymbol{u}^T (D_0 - \gamma D_1)^T (D_0 - \gamma D_1)\boldsymbol{u} + 2\boldsymbol{u}^T (D_0 - \gamma D_1)^T \mathbf{1}_N h + h^2 N
\end{aligned} \tag{3.21}$$

We can find the solution of first minimization problem over the parameter h by taking derivative with respect to parameter h and equate to zero:

$$2\boldsymbol{u}^T (D_0 - \gamma D_1)^T \mathbf{1}_N + 2hN = 0 \tag{3.22}$$

which leads to the optimal value of h as following:

$$h_{opt}(\gamma, \boldsymbol{u}) = -\frac{1}{N} \mathbf{1}_N^T (D_0 - \gamma D_1)\boldsymbol{u} \tag{3.23}$$

Subproblem 2. Once its optimal value is identified, h can be factored out of the optimization by substituting h_{opt} into Q. This new cost function is denoted as Q_2, and it represents the minimum of Q over h as follows:

$$\begin{aligned}
Q_1(\gamma, \boldsymbol{u}, h_{opt}) &= \boldsymbol{u}^T (D_0 - \gamma D_1)^T (D_0 - \gamma D_1)\boldsymbol{u} + 2\boldsymbol{u}^T (D_0 - \gamma D_1)^T \mathbf{1}_N h + h^2 N \\
&= \boldsymbol{u}^T (D_0 - \gamma D_1)^T (D_0 - \gamma D_1)\boldsymbol{u} - \frac{1}{N} \boldsymbol{u}^T (D_0 - \gamma D_1)^T \mathbf{1}_N \mathbf{1}_N^T (D_0 - \gamma D_1)\boldsymbol{u} \\
&= \boldsymbol{u}^T (D_0 - \gamma D_1)^T (I_N - \frac{1}{N} \mathbf{1}_N \mathbf{1}_N^T)(D_0 - \gamma D_1)\boldsymbol{u} \\
&= \boldsymbol{u}^T (D_0 - \gamma D_1)^T Z (D_0 - \gamma D_1)\boldsymbol{u} \\
&= \boldsymbol{u}^T \left(D_0^T Z D_0 - \gamma D_0^T Z D_1 - \gamma D_1^T Z D_0 + \gamma^2 D_1^T Z D_1 \right) \boldsymbol{u} \\
&= \boldsymbol{u}^T \left(C_0 + \gamma C_1 + \gamma^2 C_2 \right) \boldsymbol{u} \\
&= Q_2(\gamma, \boldsymbol{u})
\end{aligned} \tag{3.24}$$

Shortly, Q_2 can be expressed as a function of γ and $\boldsymbol{u}$:

$$Q_2(\gamma, \boldsymbol{u}) = \boldsymbol{u}^T \left(C_0 + \gamma C_1 + \gamma^2 C_2 \right) \boldsymbol{u} \tag{3.25}$$

where $C_0 = D_0^T Z D_0$, $C_1 = -D_0^T Z D_1 - D_1^T Z D_0$, $C_2 = D_1^T Z D_1$ and $Z = I_N - \frac{1}{N} 1_{N \times N}$.

The second problem is then defined as a minimization over $\boldsymbol{u}$ conditioned on γ:

$$\begin{aligned} \underset{\boldsymbol{u}}{\text{minimize}} \quad & \boldsymbol{u}^T \left(C_0 + \gamma C_1 + \gamma^2 C_2 \right) \boldsymbol{u} \\ \text{subject to} \quad & \boldsymbol{u}^T B \boldsymbol{u} = 1, \text{ and } \boldsymbol{u}^T \boldsymbol{d} > 0 \end{aligned} \tag{3.26}$$

The Lagrangian for the above problem is:

$$\mathcal{L}(\boldsymbol{u}, \lambda; \gamma) = \boldsymbol{u}^T \left(C_0 + \gamma C_1 + \gamma^2 C_2 \right) \boldsymbol{u} - \lambda (\boldsymbol{u}^T B \boldsymbol{u} - 1) \tag{3.27}$$

where $\lambda \in \mathbb{R}$ is the Lagrange multiplier. Note that we exclude the strict inequality constraint to be able to apply KKT conditions, but we will find a feasible solution that also satisfies the strict inequality at the end.

If we take derivative of the Lagrangian and equate the zero:

$$\begin{aligned} \frac{\partial \mathcal{L}}{\partial \boldsymbol{u}} = 2 C_0 \boldsymbol{u} + 2 \gamma C_1 \boldsymbol{u} + 2 \gamma^2 C_2 \boldsymbol{u} - 2 \lambda B \boldsymbol{u} &= \boldsymbol{0}_2 \\ \left(C_0 + \gamma C_1 \ + \gamma^2 C_2 - \lambda B \right) \boldsymbol{u} &= \boldsymbol{0}_2 \end{aligned} \tag{3.28}$$

Then, we obtain following generalized eigenvalue problem (GEP), where λ is the eigenvalue and $\boldsymbol{u}$ is the eigenvector of the problem:

$$\left(C_0 + \gamma C_1 + \gamma^2 C_2 \right) \boldsymbol{u} = \lambda B \boldsymbol{u} \tag{3.29}$$

We can apply the constraints of the problem with KKT conditions as in the following steps. If we multiply the Equation 3.29 with $\boldsymbol{u}_0^T$ from the left, where $\boldsymbol{u}_0$ is a feasible solution:

$$\underbrace{\boldsymbol{u}_0^T \left(C_0 + \gamma C_1 + \gamma^2 C_2 \right) \boldsymbol{u}_0}_{= Q_2(\gamma, \boldsymbol{u}_0)} = \lambda \underbrace{\boldsymbol{u}_0^T B \boldsymbol{u}_0}_{=1} \tag{3.30}$$

Since $Q_2(\gamma, \boldsymbol{u}_0) \geq 0$, we are only interested in non-negative λ values for the solution.

Then, if we denote the matrix $C_0+\gamma C_1+\gamma^2 C_2$ with a matrix $G(\gamma)$ as a function of γ, we can see that $G(\gamma)$ should be positive definite or positive semi-definite. We consider two possible scenarios:

- If $G(\gamma)$ is positive definite:
  Since eigenvalues of the matrix B are $(-2, 2)$, eigenvalues of the GEP will include one negative and one positive value by the Sylvester's Law of Inertia. Therefore, as there will be only one positive eigenvalue, the maximum eigenvalue (λ_{max}) will be the solution.

- If $G(\gamma)$ is positive semi-definite:
  As at least one eigenvalue should be zero to have positive semi-definite matrix, there will be three different sign configurations of eigenvalues; $(\lambda_1, \lambda_2) = (-, 0), (0, 0), (0, +)$. For the $(-, 0)$ case, 0 will be the solution (again it is the maximum eigenvalue λ_{max}). We can exclude the $(0, 0)$ case since it yields $Q_2(\gamma, \boldsymbol{u}_0) = 0$ which means that the objective value is 0 for each γ, which is not possible. For the $(0, +)$ case, the maximum eigenvalue (λ_{max}) will be the solution. As stated in the paper [35], infinitesimal variation of the data that would make $G(\gamma)$ positive definite matrix yields $(-, +)$ configuration, therefore the eigenvalue corresponding to positive eigenvalue after infinitesimal variation (again λ_{max}) should be the solution.

We can see from above that for both scenarios the largest eigenvalue λ_{max} is the solution, which means $Q_3(\gamma) = \lambda_{max}\left(C_0 + \gamma C_1 + \gamma^2 C_2, B\right)$. Additionally, in order to satisfy $\boldsymbol{u}^T B \boldsymbol{u} = 1$ and $\boldsymbol{u}^T d > 0$ constraints, we can choose the optimal value for the eigenvector $\boldsymbol{u}_{opt}$ as the scaling of the eigenvector $\boldsymbol{u}_{max}$ corresponding to the eigenvalue λ_{max}:

$$\boldsymbol{u}_{opt}(\gamma) = \frac{\text{sign}(\boldsymbol{u}_{max}^T \boldsymbol{d})}{\sqrt{\boldsymbol{u}_{max}^T B \boldsymbol{u}_{max}}} \boldsymbol{u}_{max} \tag{3.31}$$

Therefore, the minimum value of the function Q_2 is the maximum eigenvalue λ_{max} of the generalized eigenvalue problem (GEP) and the minimum is attained at the respective eigenvector $\boldsymbol{u}_{max}$.

Subproblem 3. Once $\boldsymbol{u}_{opt}$ is identified, it is factored out by substitution into Q_2. This results in a new cost function denoted as Q_3 depending only on γ that controls the location of the ellipse center:

$$Q_3(\gamma) = \lambda_{max}\left(C_0 + \gamma C_1 + \gamma^2 C_2, B\right) \tag{3.32}$$

To derive function Q_3, we can find λ_{max} as a function of γ with the following steps.

- First, we write the characteristic polynomial to find possible values of λ:

$$\det\left(C_0 + \gamma C_1 + \gamma^2 C_2 - \lambda B\right) = 0 \tag{3.33}$$

- As D_0 matrix has one column of zeros, C_0, C_1 and C_2 matrices have following special structures where we denote non-zero elements of the matrices with $\times$:

$$\det\left(\begin{bmatrix}\times & \times\\ \times & \times\end{bmatrix} + \gamma\begin{bmatrix}\times & \times\\ \times & 0\end{bmatrix} + \gamma^2\begin{bmatrix}\times & 0\\ 0 & 0\end{bmatrix} - \lambda\begin{bmatrix}0 & 2\\ 2 & 0\end{bmatrix}\right) = 0 \tag{3.34}$$

- If we calculate the above determinant, we get following equation where we denote the element in i^{th} row and j^{th} column of a matrix with the subscript ij:

$$4\lambda^2 + (t_1 + \gamma t_2)\lambda + \gamma^2 t_3 + \gamma t_4 + t_5 = 0 \tag{3.35}$$

where

$$\begin{aligned} t_1 &= 2(C_{0,12} + C_{0,21}) \\ t_2 &= 2(C_{1,12} + C_{1,21}) \\ t_3 &= C_{0,22}C_{2,11} - C_{1,12}C_{1,21} \\ t_4 &= C_{0,22}C_{1,11} - C_{0,12}C_{1,21} - C_{0,21}C_{1,12} \\ t_5 &= C_{0,11}C_{0,22} - C_{0,12}C_{0,21} \end{aligned} \tag{3.36}$$

- As Equation 3.35 is a polynomial of second degree with respect to λ, we can choose the maximum root of the polynomial as λ_{max}:

$$\lambda_{max}(\gamma) = \frac{-(t_1 + \gamma t_2) + \sqrt{(t_1 + \gamma t_2)^2 - 16(\gamma^2 t_3 + \gamma t_4 + t_5)}}{8} \tag{3.37}$$

  Then, $Q_3(\gamma) = \lambda_{max}(\gamma)$.

Thus, solving Eq. 3.18 is equivalent to solving the problem below:

$$\underset{\gamma}{\text{minimize}}\ Q_3(\gamma) \tag{3.38}$$

In other words, overall problem is reduced to a one-dimensional minimum search where we seek a solution for each γ and find the one giving minimum λ_{max}:

$$Q_1(\gamma^*, \boldsymbol{u}^*, h^*) = Q_3(\gamma^*) \tag{3.39}$$

where the superscript * represents the solution yielding optimum result. Instead of one-dimensional minimum search, we can also directly derive the analytical solution for γ. We can find the possible solutions for γ by taking derivative of the $Q_3(\gamma)$ with respect to γ and equating the zero. Then, we obtain following possible solutions:

$$\gamma_{1,2} = \frac{-(t_1 t_2 - 8t_4) \pm \sqrt{(t_1 t_2 - 8t_4)^2 - 4(t_2^2 - 16t_3)(t_1 t_2 t_4 - t_2^2 t_5 - 4t_4^2)/t_3}}{t_2^2 - 16t_3} \tag{3.40}$$

Lastly, we choose the one giving the minimum function value among two solutions:

$$\gamma^* = \underset{\gamma \in \{\gamma_1, \gamma_2\}}{\operatorname{argmin}} Q_3(\gamma) \tag{3.41}$$

.

Once the optimum value is identified, the remaining parameters can be extracted from γ^* as follows:

$$\begin{aligned} \boldsymbol{u}^* &= \boldsymbol{u}_{opt}(\gamma^*) \\ h^* &= h_{opt}(\gamma^*, \boldsymbol{u}^*) \\ A^* &= \begin{bmatrix} u_1^* & 0 \\ 0 & u_2^* \end{bmatrix} \\ \boldsymbol{x}_c^* &= \begin{bmatrix} \gamma^* q & 0 \end{bmatrix} \\ g^* &= h^* - \gamma^{*2} q^2 \boldsymbol{u}^{*T} \boldsymbol{d} \end{aligned} \tag{3.42}$$

These estimated parameters include all information required to find features of the rotated ellipse, which later will be used to find the parameters in Equation 3.2.

Dictionary-based ellipse identification

Inherent noise in bSSFP measurements can limit the accuracy of ellipse fits when lower N is prescribed. This in turn can degrade the quality of estimates particularly for T_1 and T_2 values. To improve ellipse fits, here we employ a dictionary-based ellipse identification procedure. To construct a dictionary, we first simulate bSSFP signal parameters M, a and b according to Eq. 3.2. A broad range of T_1, T_2 values are considered, given the TR, TE and α of the bSSFP sequence. The dictionary only contains the following ellipse properties: the semi-axes radii and the distance between the ellipse center and the origin, calculated according to Eqs. 3.4-3.5. Since these properties are not affected by main-field inhomogeneity, we do not consider off-resonance in the simulations. The resulting dictionary

contains semi-axes radii and center distance properties for all pairs of T_1-T_2 examined.

For identification, a comparison is performed between properties of the dictionary ellipses and the fit ellipse for S. The semi-axes radii of the fit ellipse can be extracted from the solution in Eq. 3.42 as follows:

- Semi-minor axis: $[\sqrt{-\frac{g^*}{u_1^*}}, 0]$ (3.43)
- Semi-minor radius: $r_{min} = \sqrt{-\frac{g^*}{u_1^*}}$ (3.44)
- Semi-major axis: $[0, \sqrt{-\frac{g^*}{u_3^*}}]$ (3.45)
- Semi-major radius: $r_{maj} = \sqrt{-\frac{g^*}{u_3^*}}$ (3.46)

Meanwhile, the center distance can be directly calculated from the x_c^* in Eq. 3.42. The summed $\ell_2 - norm$ distance between the properties of the dictionary and fit elllipse's are computed. To prevent biases due to differences in signal scales, all ellipse properties are normalized by the cross-point distances (i.e. $|M|$ for the dictionary ellipse, $|q|$ for the fit ellipse) prior to distance calculation. The dictionary ellipse that minimizes the distance to the fit ellipse is then selected as the final ellipse estimate.

Parameter estimation

Given the center x_c^* and semi-axes radii r_{min} and r_{maj} of the final ellipse estimate, we can compute the parameters in Eq. 3.2 as follows:

$$\begin{aligned} b^* &= \frac{-r_{min}x_c^* + r_{maj}\sqrt{x_c^{*2} - r_{min}^2 + r_{maj}^2}}{x_c^{*2} + r_{maj}^2} \\ a^* &= \frac{r_{maj}}{x_c^*\sqrt{1-b^{*2}} + r_{maj}b^*} \\ M^* &= \frac{x_c^*(1-b^{*2})}{1-a^*b^*} \end{aligned} \tag{3.47}$$

Once (M^*, a^*, b^*) are known, T_1 and T_2 values can be derived analytically [31]:

$$\begin{aligned} T_1 &= -\frac{TR}{\ln \frac{a^*(1+\cos\alpha - a^* b^* \cos\alpha) - b^*}{a^*(1+\cos\alpha - a^* b^*) - b^* \cos\alpha}} \\ T_2 &= -\frac{TR}{\ln a^*} \end{aligned} \tag{3.48}$$

Note that M^* serves as an estimate for the banding-free image as it does not show any off-resonance dependency [15]. Meanwhile, given ($\tilde{x}_i$, x_c^*, r_{min}, b^*, $\Delta\theta_i$), off-resonance in each voxel can be calculated via ordinary least squares solution of the following system of equations:

$$\begin{bmatrix} \cos(\Delta\theta_1) & \sin(\Delta\theta_1) \\ \vdots & \vdots \\ \cos(\Delta\theta_N) & \sin(\Delta\theta_N) \end{bmatrix} \begin{bmatrix} K_1 \\ K_2 \end{bmatrix} = \begin{bmatrix} \cos(\theta_1) \\ \vdots \\ \cos(\theta_N) \end{bmatrix} \tag{3.49}$$

where

$$\cos(\theta_i) = \frac{\cos\left(\frac{\tilde{x}_i - x_c^*}{r_{min}}\right) - b^*}{\cos\left(\frac{\tilde{x}_i - x_c^*}{r_{min}}\right) b^* - 1} \tag{3.50}$$

Lastly, $\theta_0 = \tan^{-1}(K_2/K_1)$. While this calculation is similar to the fourth step of reconstruction in PLANET [31], it differs in that $cos(\theta_i)$ is directly calculated.

3.2.4 Contributions

The novel contributions of this study are summarized below:

- We introduce an ellipse fitting procedure with a geometric constraint on the ellipse's central line for relaxation parameter estimation with phase-cycled bSSFP MRI.
- We derive an analytical solution for the constrained ellipse fit to avoid brute-force search or iterative optimization approaches.
- We introduce a dictionary-based identification procedure on the ellipse fits

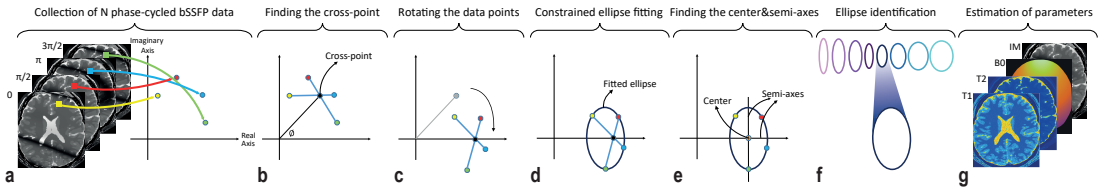

Figure 3.2: Flowchart of the proposed constrained ellipse fitting (CELF) approach. For a given voxel, the ESM model observes that each phase-cycled bSSFP measurement should project to an ellipse in the complex plane. In CELF: (b) The ellipse cross-point is first computed via the geometric solution to identify the central line of the ellipse; (c) Measurement points are back-rotated by the angle between central line and real-axis; (d) The prior knowledge of the cross-point is then used to enable constrained ellipse fitting with as few as N=4; (e) Geometric properties of the fit ellipse including center and semi-axes are extracted; (f) A dictionary-based ellipse identification is performed to improve accuracy; (g) Lastly, parameters estimates are obtained based on the geometric properties of the final ellipse fit.

to further improve estimation accuracy. Identification is performed on the ellipses as opposed to raw bSSFP signals for reliability against off-resonance.

- We demonstrate that the proposed formulation enables estimation of T_1 and T_2 parameters with as few as N=4 phase-cycled acquisitions.

3.3 Methods

3.3.1 Constrained Ellipse Fitting

The constrained ellipse fitting method requires the knowledge of the central line of the ellipse. For ellipses spanned by phase-cycled bSSFP signals, it can be observed that both the ellipse center and the cross-point lie on the semi-minor axis. It can also be observed that the semi-minor axis in the ellipse for S_{base} and the ellipse for S both pass through the origin (see Fig. 3.1a-b). Thus, the semi-minor axis is a line segment on the central line, and the central line can be identified by finding the cross-point(see Fig. 3.1c). Here we found the cross-point q via the geometric solution described in Eq. 3.8. Once the central line

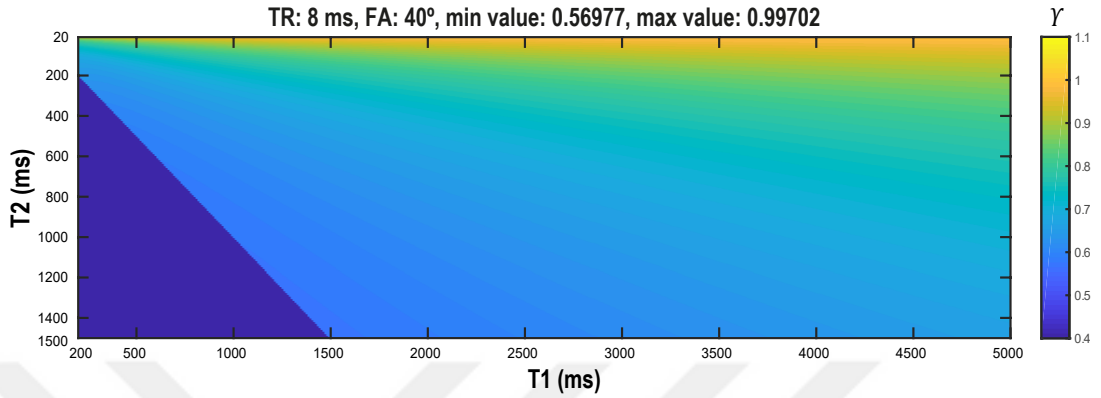

Figure 3.3: To determine the possible range of γ, bSSFP signal parameters were simulated. Representative results are displayed for a TR of 8 ms, a flip angle of 40^o, $T_1 \in [200\ 5000]$ ms and $T_2 \in [10\ 1500]$ ms such that $T_1 \geq T_2$.

was identified, all data points were back-rotated around the origin by an angle ϕ, i.e. the angle that the central line makes with the real axis. This corresponds to rotating the ellipse for S into a vertically-oriented form such that its center is on the real axis.

Afterwards, the constrained ellipse fitting problem is formulated based on the cross-point q. Solving the optimization problem in Eq. 3.38 yields γ^* in Eq. 3.42. Here we employed an analytical solution for γ^*, which inherently disregards measurement noise. Yet, excessive noise can cause complex valued roots $\gamma_{1,2}$ (Eq. 3.40). In this case, we instead selected γ through a bounded search to minimize λ_{max}. Note that the ellipse center given by $x_c = M\frac{1-ab}{1-b^2}$ can also be expressed in terms of the cross-point as $x_c = \gamma q$. Since q corresponds to M, γ should ideally equal $\frac{1-ab}{1-b^2}$. To find the possible range of γ, we computed its value for all possible values of signal parameters a and b where T_1 ranged from 200 to 5000 ms, T_2 ranged from 10 to 1500 ms, flip angle ranged from 20^o to 80^o, and TR ranged from 4 to 10 ms (see Fig. 3.3-3.6 for set of example range of γ where TR of {4,8} ms, and flip angle of $\{20^o,40^o\}$). Hence, the range of γ used in bounded search was restricted in [0.5 1].

The constrained formulation allows for an ellipse with with as few as N=4. Still, the quality of the ellipse fit can be degraded for relatively low N or high levels of noise. To improve noise resilience, here we employed a dictionary-based

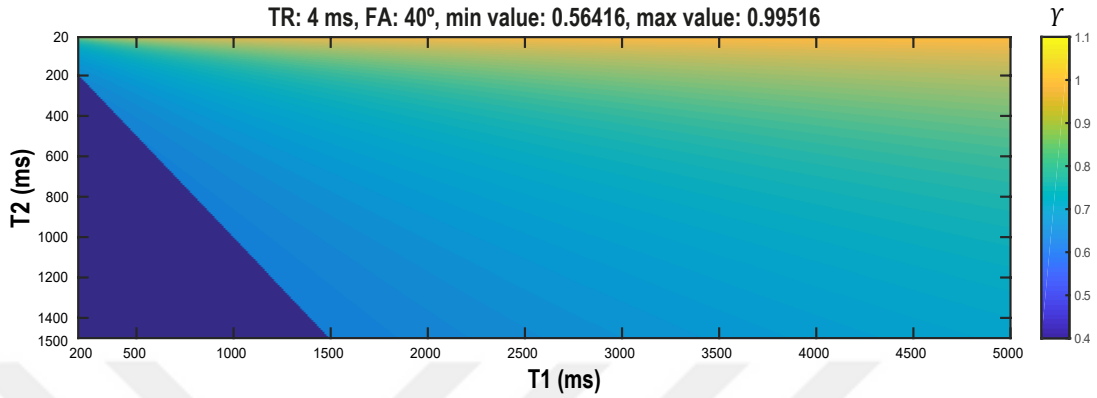

Figure 3.4: To determine the possible range of γ, bSSFP signal parameters were simulated. Representative results are displayed for a TR of 4 ms, a flip angle of 40^o, $T_1 \in [200\ 5000]$ ms and $T_2 \in [10\ 1500]$ ms such that $T_1 \geq T_2$.

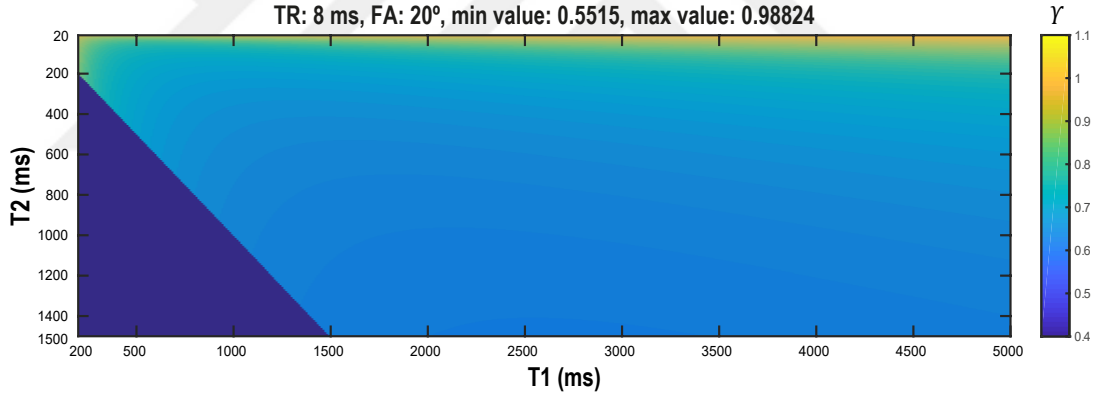

Figure 3.5: To determine the possible range of γ, bSSFP signal parameters were simulated. Representative results are displayed for a TR of 8 ms, a flip angle of 20^o, $T_1 \in [200\ 5000]$ ms and $T_2 \in [10\ 1500]$ ms such that $T_1 \geq T_2$.

ellipse identification procedure. Ellipses were simulated for all possible pairs (T_1,T_2), where T_1 ranged from 50 to 5000 ms in 5-ms steps, and T_2 ranged from 10 to 500 ms in 1-ms steps and from 500 to 1500 ms in 5-ms steps. Simulated M, a, b values were used to calculate the semi-axes radii and the distance between the ellipse center and the origin (Eqs. 3.4-3.5). The dictionary ellipse that had the most similar properties to the fit ellipse was selected. The known T_1 and T_2 values of the selected dictionary ellipse were designated as the final parameter estimates.

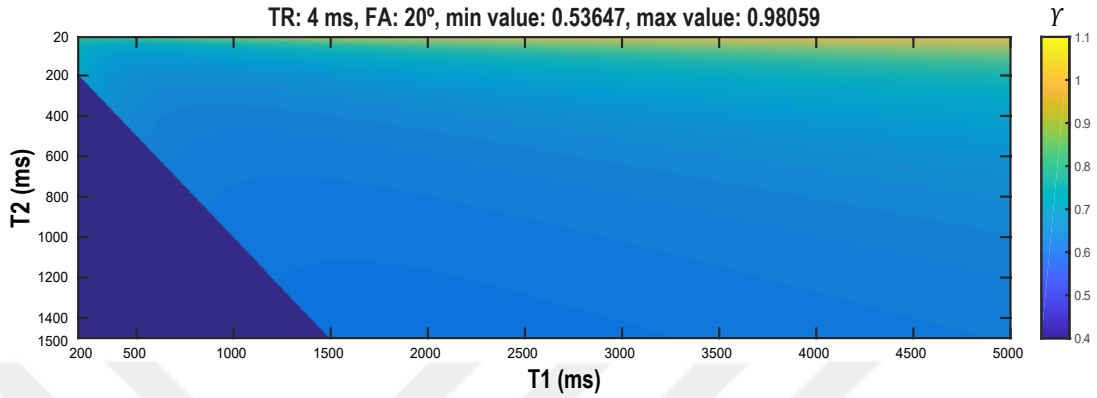

Figure 3.6: To determine the possible range of γ, bSSFP signal parameters were simulated. Representative results are displayed for a TR of 4 ms, a flip angle of 20^o, $T_1 \in [200\ 5000]$ ms and $T_2 \in [10\ 1500]$ ms such that $T_1 \geq T_2$.

3.3.2 Direct Ellipse Fitting

PLANET was used for direct ellipse fitting as described in Ref. [31]. In PLANET, the ellipse for S is back-rotated to vertical orientation with a rotation angle $\varphi_{rot} = 0.5 \tan^{-1}(\nu_2/(\nu_1 - \nu_3))$. Here, we observed that φ_{rot} may not always assure a strict vertical orientation due to measurement noise. We reasoned that the rotation angle that back-rotates the fit ellipse such that ellipse center is on the x-axis is instead ϕ. Therefore, we implemented two variants of PLANET: the original method with φ_{rot} rotation (PLANET$_1$), another with ϕ rotation (PLANET$_2$). Since we generally observed that PLANET$_2$ is less prone to estimation errors, here we presented results from PLANET$_2$. Comparison of results obtained with two variants of PLANET in simulations are given in Fig. 3.9. Note that the explicit vertical-orientation constraint in CELF ensures that φ_{rot} and ϕ are identical.

3.3.3 Simulations

To comprehensively assess parameter estimation performance, two separate simulations were performed. First, phase-cycled bSSFP signals were simulated for

nine different tissues under varying noise levels. The following tissues were considered: fat, bone marrow, liver, white matter, myocardium, vessels, gray matter, muscle and CSF. The relaxation times of the tissues at 3T were selected according to Ref [36], as listed in Table 3.1. $TR = 8$ms, $TE = 4$ms, flip angle $\alpha = 40^o$ and $N = \{6, 8\}$ were assumed. Bi-variate Gaussian noise was added to simulated signals to attain SNR values in the range [20, 100]. Note that these SNR values were calculated separately for each tissue, so at a fixed SNR level the standard deviation of added noise varied across tissues with respect to the level of tissue signal. SNR was taken as defined in previous studies [14, 31]:

$$\text{SNR} = \frac{\sum_{n=1}^{N} |S_n|}{N\sigma} \tag{3.51}$$

where S_n denotes the signal for the n^{th} phase-cycled acquisition, σ is the standard deviation of noise. Monte-Carlo simulations were repeated 10000 times with independent noise instances. At each instance, θ_0 was chosen from uniformly distributed values between $-\pi$ and π. T_1 and T_2 estimation was performed via constrained ellipse fitting (CELF) and direct ellipse fitting (PLANET$_2$). Performance was quantified as mean absolute percentage error (MAPE):

$$\text{MAPE}(\%) = \frac{100}{K} \sum_{k=1}^{K} \left| \frac{T^k_{i,true} - T^k_{i,estimated}}{T^k_{i,true}} \right| \tag{3.52}$$

where K is the number of repetitions and T^k_i is the value of T_i ($i \in 1, 2$) in the k^{th} repeat.

Second, phase-cycled bSSFP signals were simulated for the same set of tissues for varying flip angles and off-resonance. $TR = 8$ms, $TE = 4$ms, flip angle $\alpha = 20^o - 60^o$, off-resonance from -62.5 Hz to 62.5 Hz corresponding to range between $-0.5/TR$ and $0.5/TR$, and $N = \{4, 6, 8\}$ were considered. Bi-variate Gaussian noise was added to simulated signals to attain an SNR value of 200. For this simulation, SNR was defined with respect to CSF that is the tissue with the maximum signal level and the same standard deviation of noise was assumed across tissues. Simulations were repeated 20 times with independent noise instances. T_1, T_2, and off-resonance estimations were performed via CELF

and PLANET$_2$. Performance was shown visually.

Table 3.1: T_1 and T_2 values of various tissues at 3T

Tissue	T_1 (ms)	T_2 (ms)
Fat	350	130
Bone marrow	370	50
Liver	800	40
White Matter	1000	80
Myocardium	1150	45
Vessels	1200	50
Gray Matter	1300	110
Muscle	1400	30
CSF	4000	1000

3.3.4 Experiments

Phantom and in vivo experiments were performed on a 3T whole-body scanner (Siemens Magnetom Trio, Erlangen, Germany) equipped with gradients of maximum strength 45 mT/m and maximum slew rate 200 T/m/s. A 3D Cartesian sequence was used for phase-cycled bSSFP acquisitions, and consecutive acquisitions were collected without delay. Standard volumetric shimming was performed at the beginning of the scan session, and the shim was unaltered thereafter. For comparison, reference T_1 and T_2 maps were obtained using gold-standard sequences as close as possible to the central cross-section of the bSSFP acquisitions. B_1 maps were acquired to estimate the actual flip angle for a prescribed nominal angle across the field-of-view (FOV). B_0 maps were acquired to account for potential drifts in the main field inhomogeneity during the session. All imaging protocols were approved by the local ethics committee at Bilkent University, and informed consent was obtained from all participants. Details of specific sequences are listed below:

- **Phantom bSSFP scans:** Phase-cycled bSSFP acquisitions of a homogeneous phantom were performed using a 12-channel head coil. The sequence parameters were a TR/TE of 8.89/4.445 ms, a flip angle of 55^o, an FOV of

175 mm × 175 mm × 120 mm, a matrix size of 128 × 128 × 40, a resolution of 1.36 mm × 1.36 mm × 3 mm, a readout bandwidth of 160 Hz/Px, and $N = 8$ phase-cycles with $\Delta\theta$ spanning $[0, 2\pi)$ in equispaced intervals. Total scan time for $N = 8$ was 6 min 32 s. A subset of acquisitions for N=8 were selected for assessments on lower N: $N = 4$ (i.e. $\Delta\theta = \{0, \pi/2, \pi, 3\pi/2\}$) and $N = 6$ (i.e. $\Delta\theta = \{0, \pi/4, \pi/2, \pi, 5\pi/4, 3\pi/2\}$).

- **In vivo bSSFP scans:** Phase-cycled bSSFP acquisitions of the brain were performed using a 32-channel head coil. The sequence parameters were a TR/TE of 8.18/4.09 ms, a flip angle of 40^o, an FOV of 256 mm × 256 mm × 120 mm, a matrix size of 256 × 256 × 30, a resolution of 1 mm × 1 mm × 4 mm, a readout bandwidth of 190 Hz/Px, and $N = 8$ phase-cycles with $\Delta\theta$ spanning $[0, 2\pi)$ in equispaced intervals. Total scan time for $N = 8$ was 8 min 40 s. A subset of acquisitions for N=8 were selected for assessments on lower N: $N = 4$ (i.e. $\Delta\theta = \{0, \pi/2, \pi, 3\pi/2\}$) and $N = 6$ (i.e. $\Delta\theta = \{0, \pi/4, \pi/2, \pi, 5\pi/4, 3\pi/2\}$).

- **Reference T_1 mapping scans:** Reference T_1 maps for the phantom were collected using a 2D turbo spin echo sequence (IR-TSE) with inversion times $TI = \{25, 50, 100, 200, 500, 1000, 2000, 4000\}$ ms, a turbo factor of 5, a TR/TE of 4500/11 ms, an FOV of 175 mm × 175 mm, a matrix size of 128 × 128, and a resolution of 1.36 mm × 1.36 mm × 5 mm. Total scan time was 16 min 24 s. Reference T_1 maps for the brain were collected using the same sequence, but with a turbo factor of 32, a TR/TE of 5000/7.1 ms, an FOV of 256 mm × 256 mm, a matrix size of 192 × 192, and a resolution of 1.33 mm × 1.33 mm × 3 mm. Total scan time was 4 min 56 s.

- **Reference T_2 mapping scans:** Reference T_2 maps for the phantom were collected using a 2D multi-echo spin echo (ME-SE) sequence with echo times $TE = \{12 : 12 : 240\}$ ms, a TR of 5000 ms, an FOV of 175 mm × 175 mm, a matrix size of 128 × 128, and a resolution of 1.36 mm × 1.36 mm × 3 mm. Reference T_2 maps for the brain were collected using the same sequence, but with an FOV of 256 mm × 256 mm, a matrix size of 128 × 128, and a resolution of 2 mm × 2 mm × 3 mm. Total scan times for both experiments were 10 min 47 s. All ME-SE T_2 maps were corrected with the EMC fit

technique proposed in Ref [37].

- B_1 **mapping scans:** B_1 field maps were acquired using the Bloch-Siegert Shift method [38] with a 6 μs 1 kHz Fermi Pulse, a TR/TE of 100/15, and with the same FOV, matrix size and resolution of corresponding bSSFP acquisitions. Total scan times per cross-section were 25 s for the phantom and 51 s for the in vivo experiment. B_1 correction was applied voxelwise while estimating T_1 and T_2 values from Eq. 3.48 by replacing the nominal flip angle α with the actual flip angle $\alpha|B_1^+|$.

- B_0 **mapping scans:** B_0 field maps were acquired with dual-echo gradient echo acquisitions with echo times $TE = \{5.19, 7.65\}$ ms, a TR of 400 ms, a matrix size of 64×64, and identical FOV to corresponding bSSFP acquisitions. Total scan time was 50 s. To check for potential changes in main field distribution due to B_0 drifts, field maps were acquired immediately prior to and after the set of N=8 bSSFP acquisitions. No major changes in the field were observed, and when correction was performed as described in Ref. [39], no significant changes occurred in the parameter estimates. Thus, correction for B_0 drift was omitted in the presented results.

The adaptive coil-combination method that produces combined complex-valued image was used to pool data across multiple receiver channels. All fitting procedures were performed voxel-wise on this combined image. Analyses were performed in MATLAB R2015b (The MathWorks, Inc., Natick, MA, USA) on a computer with Intel® Core™ i5-6500K CPU, 16 GB RAM. Run times of the proposed technique per cross-section are listed in Table 3.2. Note that as there is negligible difference between run times for $N = 4$, $N = 6$, and $N = 8$; we provide the average run time of the method for $N = 4$, $N = 6$, and $N = 8$. Run times of PLANET per cross-section are 1.2 s for phantom and 2.4 s for in vivo.

Table 3.2: Run times of CELF

Experiment	Ellipse fit	Identification	Total
Phantom	1.5 s	13.1 s	14.6 s
In vivo	3.6 s	41.5 s	45.1 s

3.4 Results

3.4.1 Simulations

Performance of the proposed method on T_1 and T_2 estimations are first evaluated with simulations. T_1 and T_2 parameters are estimated by both CELF and PLANET for various SNR levels and different number of acquisitions $N = \{6, 8\}$. Mean absolute percentage error of 10000 Monte Carlo simulations for each SNR, each tissue and each N is calculated for both T_1 and T_2 values. Results are demonstrated in Fig. 3.7 where shades of blue are used for T_1 results, and shades of red are used for T_2 results. Also, solid lines, and dashed lines are used for methods CELF and PLANET respectively. We observe for all of tissues that CELF gives better results than PLANET for both T_1 and T_2 estimates in terms of MAPE. We also observe that since PLANET does not have any restriction for values that T_1 and T_2 can take, for lower SNR cases it may give extremum results like negative results or highly overestimated results. We observe that CSF suffers the most from negative results. As SNR increases, errors of both methods converge in some tissues like bone marrow. The most distinctive results are observed in T_1 estimations for some tissues like liver, myocardium, muscle, and vessels, where their T_1/T_2 ratio are higher compared to others. We also observe that tissues with similar T_1/T_2 ratio have similar error behavior.

In the second simulation, T_1, T_2, and off-resonance are estimated by both CELF and PLANET for various off-resonance values and flip angles, and different number of acquisitions $N = \{4, 6, 8\}$. Performances of the methods are demonstrated visually, and for each tissue results are averaged over 20 simulations. Results are demonstrated in Fig. 3.8 where reference maps are given at the left most column. Note that these results are obtained for second variant of the PLANET, and to compare variants we provide results obtained from PLANET_1 and PLANET_2 in Fig. 3.9. We observe for all tissues that CELF gives better results than PLANET for both T_1, T_2, and off-resonance estimates. The most distinctive results are observed in off-resonance estimations; they are successfully estimated with CELF in all tissues for varying flip angles, while estimations with PLANET are quite

affected by SNR of the tissue. For example, PLANET estimates the off-resonance better at tissues such as fat (block at the top-left), and CSF (block at the bottom-right), as they have higher signal intensities compared to other tissues. Also, we observe that T_1 and T_2 estimations are more robust for relatively small flip angle values from 20^o to 45^o. In $N = 4$, CELF has singularity at specific off-resonance frequencies which correspond to $\theta_0 = \{-3\pi/4, -\pi/4, \pi/4, 3\pi/4\}$. This singularity occurs only at these specific angles where no data point is located on the left part of the ellipse, which leads to erroneous ellipse fitting results in the present of noise.

3.4.2 Experiments

Performance of the proposed method on T_1 and T_2 estimations are also evaluated with phantom experiments. T_1 and T_2 maps are estimated by both CELF and PLANET for different number of acquisitions $N = \{4, 6, 8\}$. Estimated maps for three consecutive cross-section are presented along with the reference map in Figure 3.10. We can see that similar estimates can be obtained with different number of acquisitions in CELF. To better demonstrate the results, estimated T_1 and T_2 values across a central line are also presented in 3.11. We observe that CELF has less variation in estimates compared to PLANET especially for the left most part of the phantom. Although variation of CELF estimates are lower than PLANET, results of both methods tend to deviate around image volume boundaries. This can be due to sharp B_0 field changes around the boundaries.

Estimated T_1, T_2, and off-resonance maps of a representative axial cross-section of the brain are shown in Figure 3.12. Corresponding phase-cycled bSSFP data acquisitions and banding-free image magnitude estimated with CELF $N = 4$ are shown in Fig. 3.13. Mean and standard deviation of estimated T_1 and T_2 values for white matter (WM), grey matter (GM), and CSF for ROIs across the central volume are presented in Table 3.3, note that ROI calculation of CSF for PLANET is not performed due to negatively estimated values inside the CSF. We observe good agreement between estimated and reference T_2 maps for WM and GM, while

we see underestimation of approximately 23%, 38%, and 37% in T_1 estimates of WM, GM, and CSF, respectively, and overestimation of approximately 40% in T_2 estimates of CSF. Considering relaxation values of the CSF reported at different studies, average of T_2 values overestimated with respect to reference T_2 is closer to previously reported T_2 values which is typically higher than 1000 ms.

Table 3.3: Estimated T_1 and T_2 values for in vivo brain images

Methods		**WM**		**GM**		**CSF**	
		T_1 (ms)	T_2 (ms)	T_1 (ms)	T_2 (ms)	T_1 (ms)	T_2 (ms)
CELF	N=8	385 ± 69	55 ± 12	659 ± 161	75 ± 23	2350 ± 747	1174 ± 413
	N=6	412 ± 81	51 ± 11	696 ± 238	73 ± 26	2512 ± 824	1210 ± 412
	N=4	418 ± 94	56 ± 14	724 ± 187	81 ± 30	2707 ± 825	1231 ± 391
PLANET	N=8	438 ± 152	58 ± 17	859 ± 383	89 ± 42	-	-
	N=6	429 ± 159	59 ± 19	827 ± 348	89 ± 47	-	-
Reference		545 ± 17	56 ± 3	1168 ± 50	81 ± 14	3734 ± 1080	825 ± 227

To demonstrate how the dictionary-based ellipse identification step improves the result, we provide an example of T_1 and T_2 estimation results obtained before and after the ellipse identification step of CELF for a cross-section of a representative subject for $N = \{4, 8\}$ in Fig. 3.14. We can observe that negative estimates or poorly estimated parts are improved with the dictionary-based ellipse identification step of CELF. Also, to show the effect of corrected off-resonance estimation step of CELF, we provide off-resonance estimation results obtained with CELF, PLANET, and PLANET combined with off-resonance calculation step of CELF for $N = \{4, 6, 8\}$ in Fig. 3.15. We can see that off-resonance estimates of PLANET are quite improved by only changing the way that $\cos(\theta_i)$ in Eq. 3.50 is calculated.

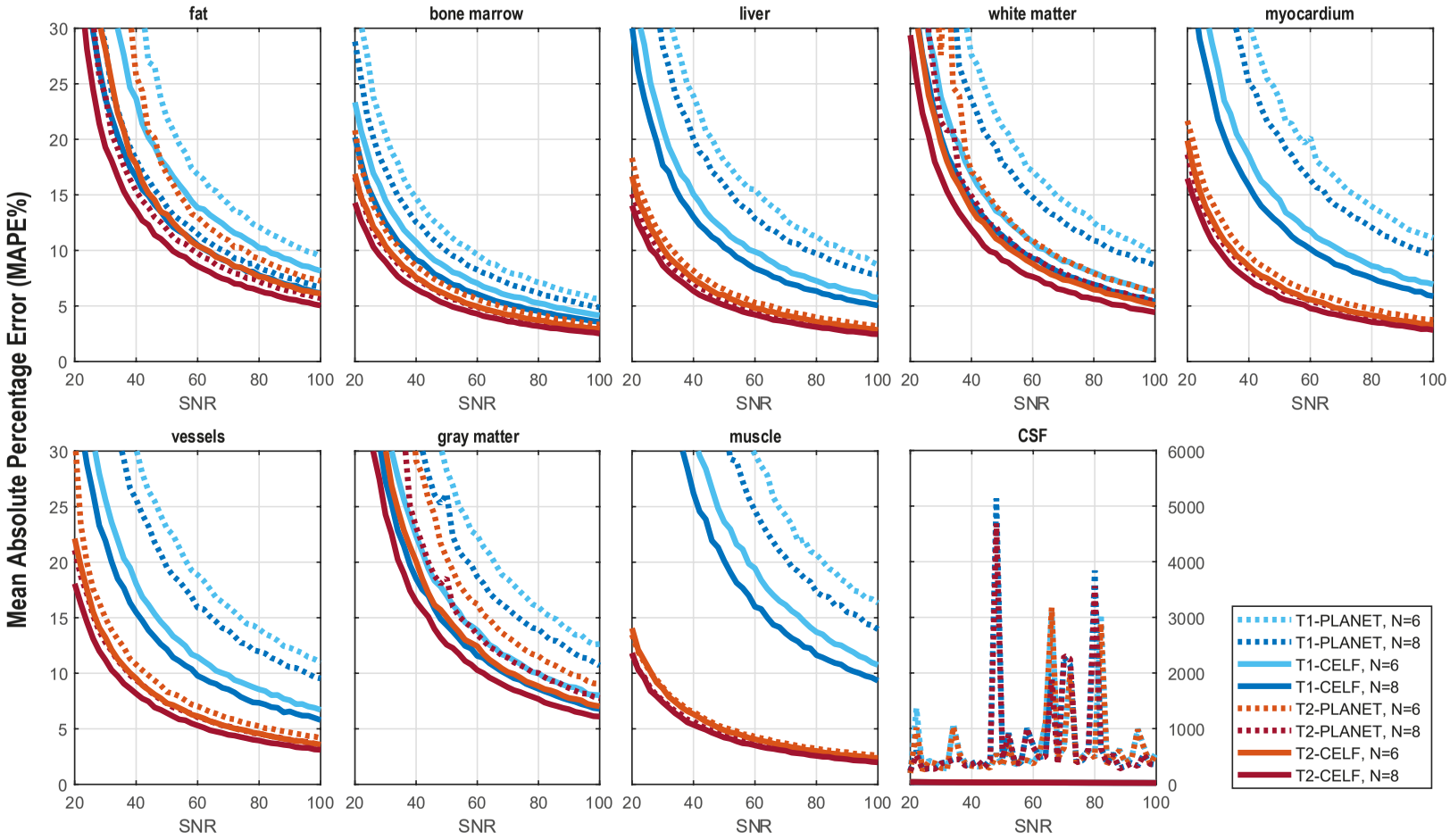

Figure 3.7: Phase-cycled bSSFP signals were simulated for nine tissues (fat, bone marrow, liver, white matter, myocardium, vessels, gray matter, muscle, and CSF) and for SNR levels varying in [20 100] in each tissue. The remaining simulation parameters were: $TR = 8$ms, $TE = 4$ms, flip angle $\alpha = 40^o$ and $N = \{6, 8\}$. CELF and PLANET were employed to estimate relaxation parameters. Errors for T_1 estimation are marked with blue lines, those for T_2 estimation are marked with red lines. Meanwhile, CELF results are shown with straight lines and PLANET results are shown with dashed lines.

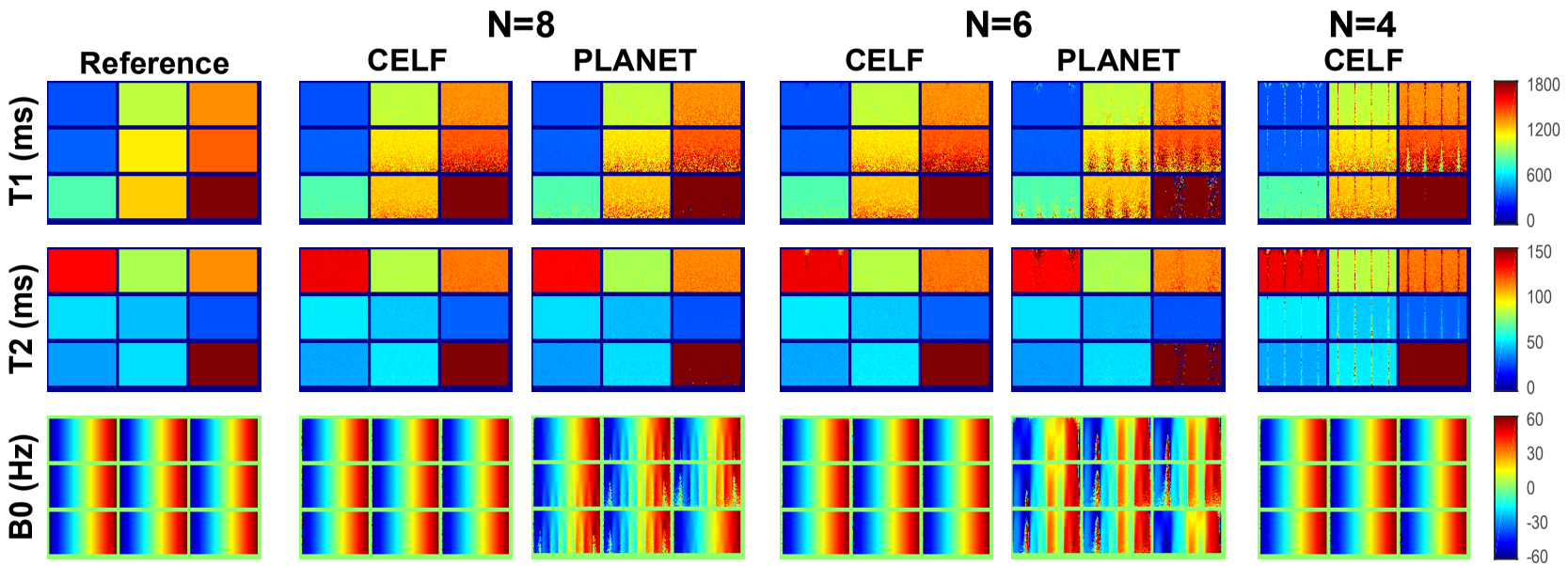

Figure 3.8: Phase-cycled bSSFP signals were simulated for nine tissue blocks (left column from top to bottom: fat, bone marrow, liver; middle column from top to bottom: white matter, myocardium, vessels; right column from top to bottom: gray matter, muscle, and CSF). In each block off-resonance varied from -62.5 Hz to 62.5 Hz ($1/2.TR$) along the horizontal axis, and flip angle varied from 20^o to 60^o along the vertical axis. Remaining parameters were: $TR = 8$ms, $TE = 4$ms, $N = \{4, 6, 8\}$, and SNR = 200 (with respect to CSF signal intensity). T_1, T_2, and off-resonance estimates via CELF and PLANET are displayed. Note that PLANET cannot compute estimates for $N = \{4\}$

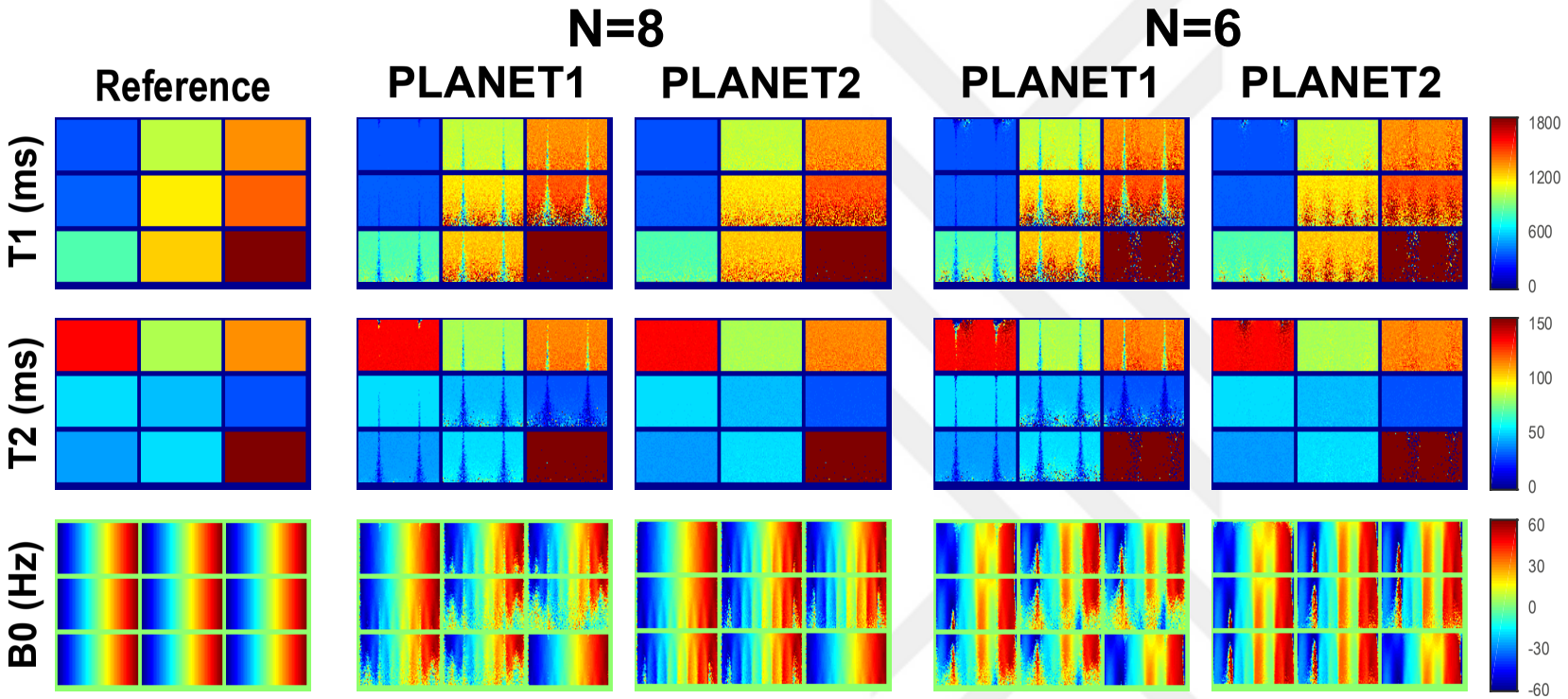

Figure 3.9: T_1, T_2, and off-resonance estimations of two variants of PLANET: PLANET_1 and PLANET_2 for various tissues (left column from top to bottom: fat, bone marrow, liver; middle column from top to bottom: white matter, myocardium, vessels; right column from top to bottom: gray matter, muscle, and CSF). Each small rectangle has varying off-resonance and flip angle values; from left to right off-resonance changes -62.5 Hz to 62.5 Hz, from top to bottom flip angle changes 20^o to 60^o.

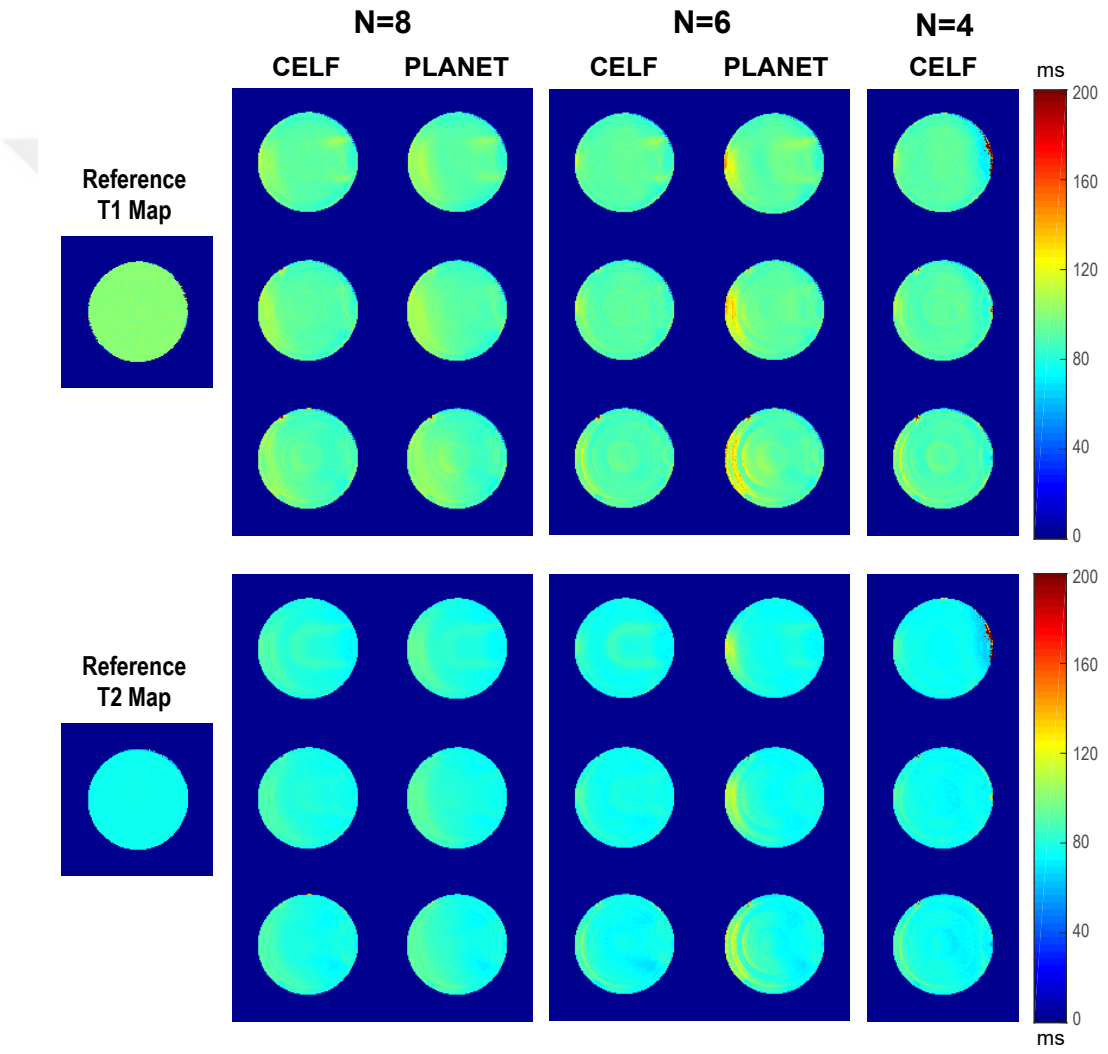

Figure 3.10: Estimated T1 and T2 maps for three cross-sections of a homogeneous phantom are shown along with the reference maps. Each column shows results of the method written top of the column.

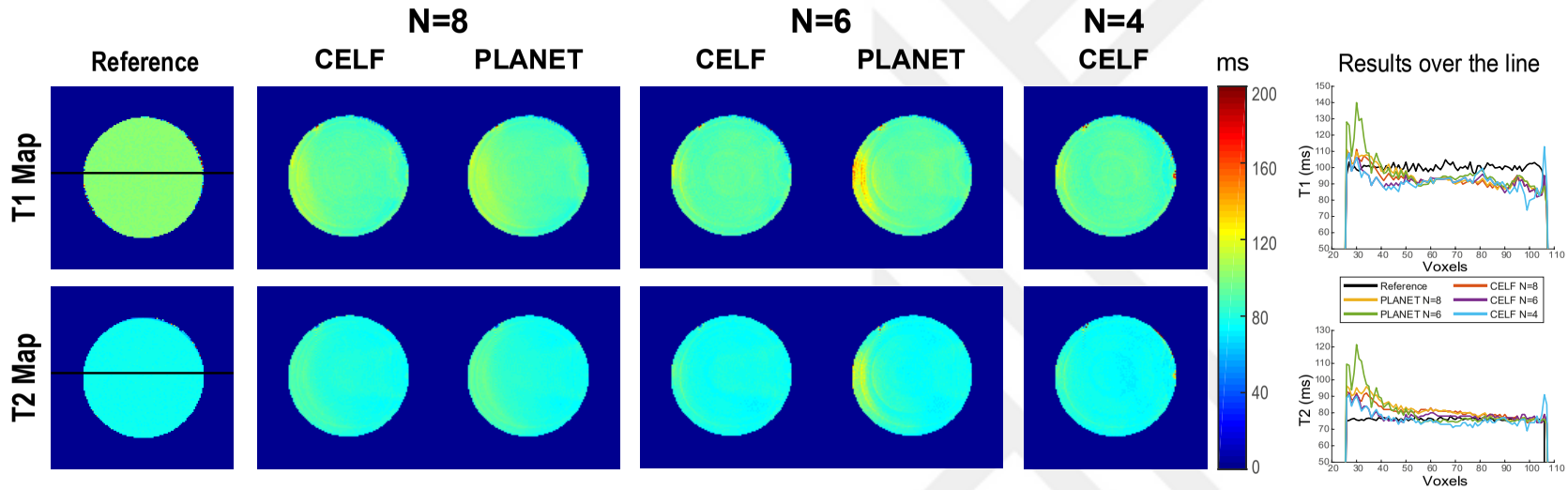

Figure 3.11: T_1 and T_2 estimation was performed with CELF and PLANET on phase-cycled bSSFP images of a homogeneous phantom. Results are shown in a representative cross-section for $N = \{4, 6, 8\}$. Note that PLANET cannot compute estimates for $N = \{4\}$. T_1 and T_2 estimates are displayed along with the reference maps from gold-standard mapping sequences. To better visualize differences among methods, variation of estimates are also plotted across a central line (black line in reference maps).

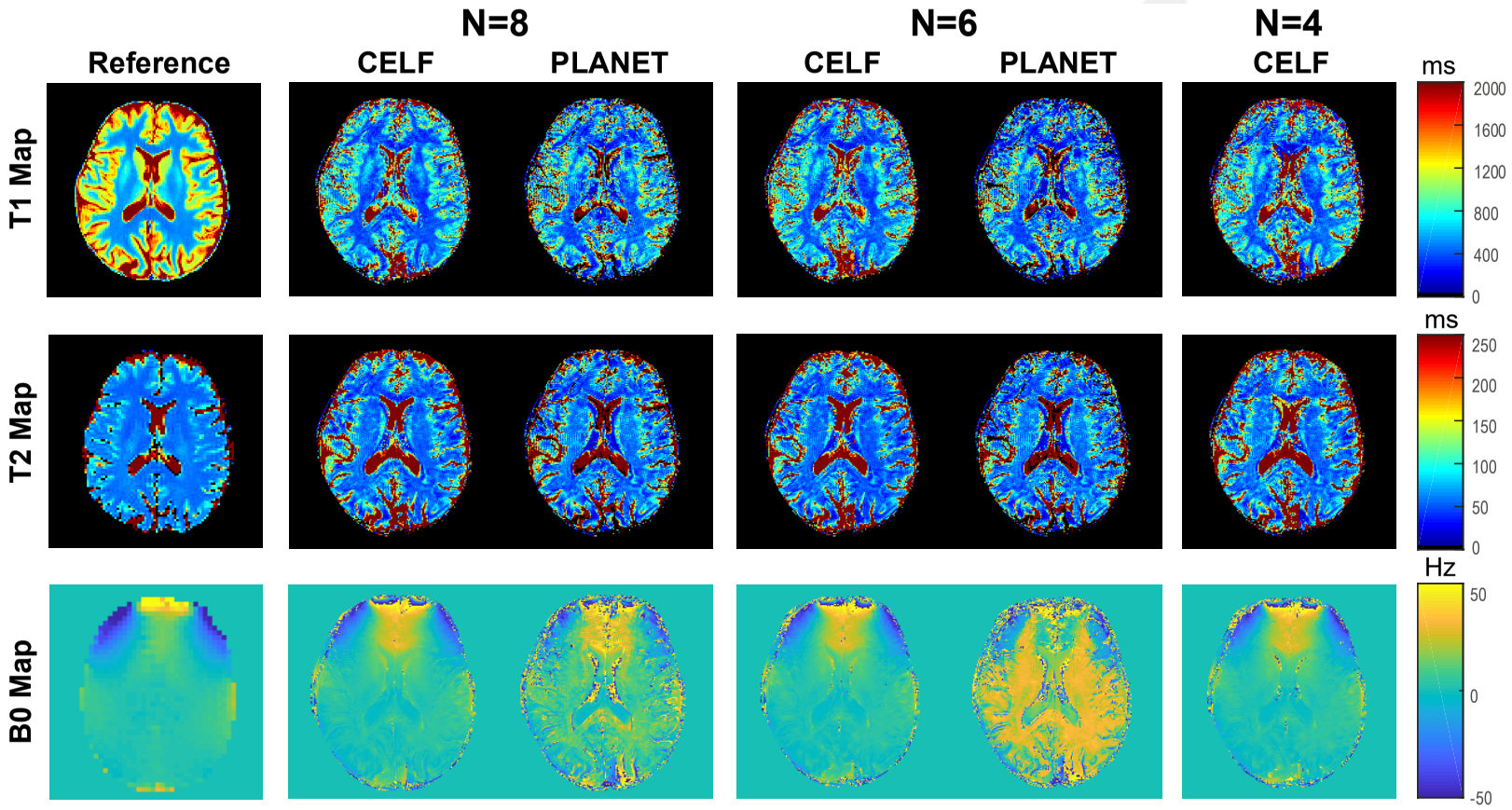

Figure 3.12: Parameter estimation was performed with CELF and PLANET on phase-cycled bSSFP images of the brain. Results are shown in a cross-section of a representative subject for $N = \{4, 6, 8\}$. Note that PLANET cannot compute estimates for $N = \{4\}$. T_1, T_2, and off-resonance estimates are displayed along with the reference maps from gold-standard mapping sequences.

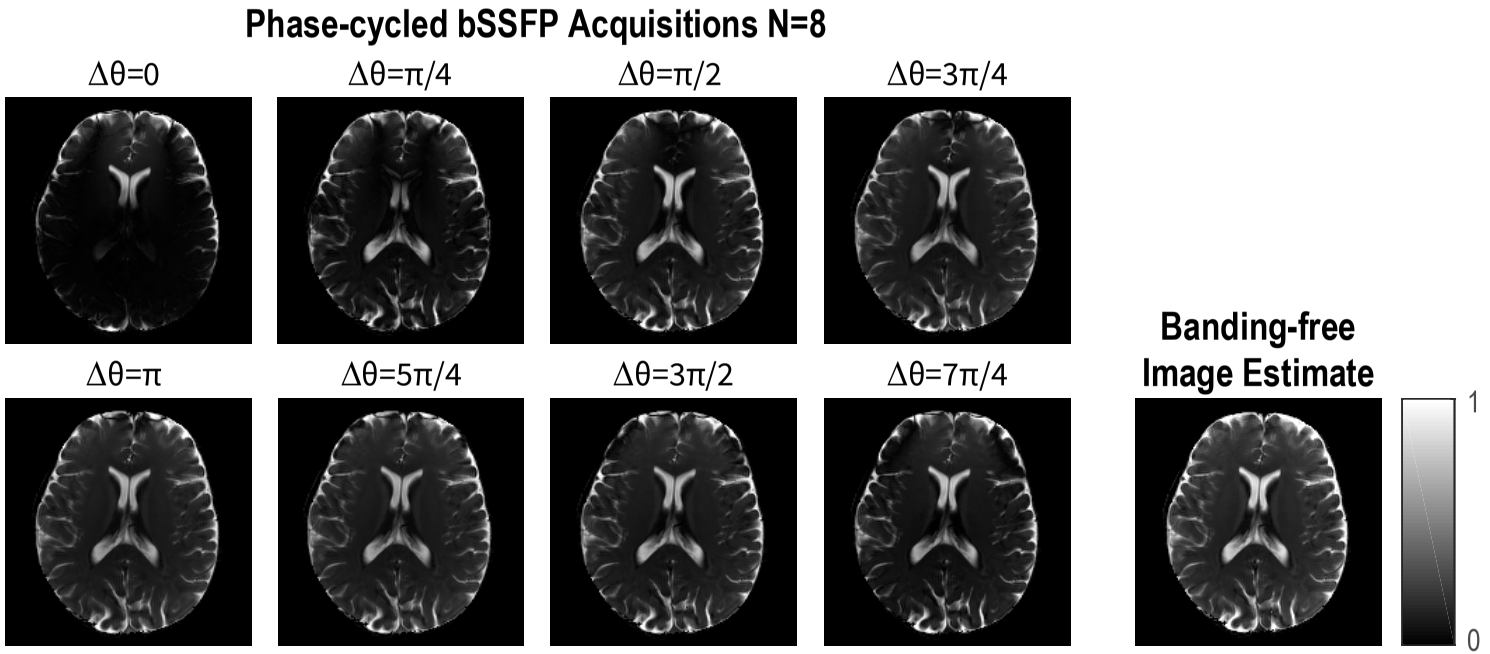

Figure 3.13: In vivo phase-cycled bSSFP acquisitions with $\Delta\theta = [0 : \pi/4 : 7\pi/4]$ are shown along with the banding-free image magnitude estimate of the CELF at $N = 4$.

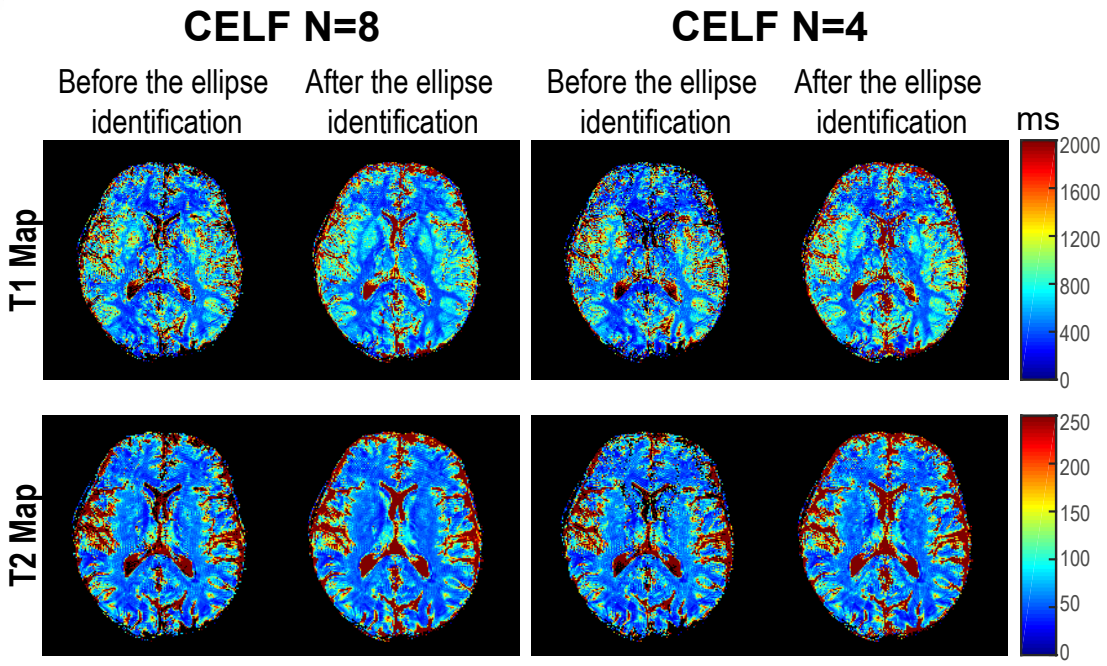

Figure 3.14: T_1 and T_2 estimations were performed with CELF on phase-cycled bSSFP images of the brain. Results obtained before and after the dictionary-based ellipse identification step are shown in a cross-section of a representative subject for $N = \{4, 8\}$.

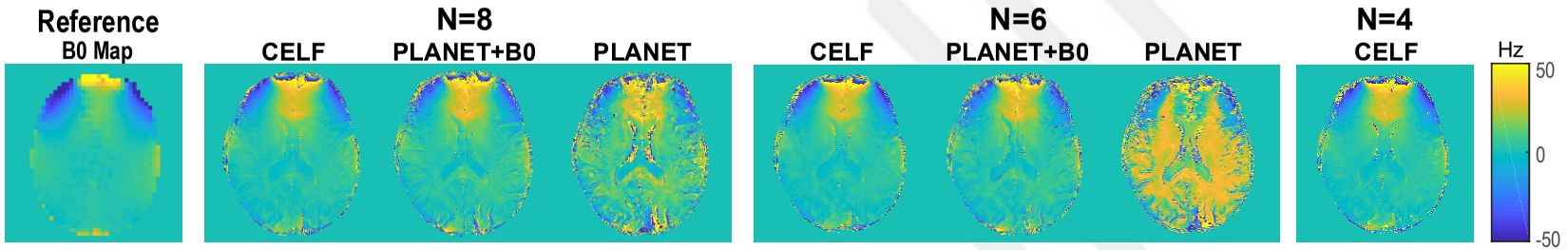

Figure 3.15: Off-resonance map estimations obtained with CELF, PLANET, PLANET with corrected off-resonance estimation step for $N = \{4, 6, 8\}$.

Chapter 4

Conclusion

Balanced steady-state free precession (bSSFP) imaging enables high scan efficiency in magnetic resonance imaging (MRI), but it differs from conventional sequences in terms of its elevated sensitivity to main field inhomogeneity and non-standard T_2/T_1-weighted tissue contrast. To address these limitations, multiple bSSFP images of the same anatomy are commonly acquired with a set of different RF phase-cycling increments. Joint processing of phase-cycled acquisitions has long been employed to suppress banding artifacts due to field inhomogeneity. Recently phase-cycled bSSFP acquisitions were also leveraged to estimate relaxation parameters based on explicit signal models. While effective, these model-based methods often require a large number of acquisitions (N≈10-16), degrading scan efficiency.

In this thesis, main contributions are constrained ellipse fitting and dictionary-based identification approaches applied for estimation of T_1 and T_2 values from phase-cycled bSSFP acquisitions. Prior knowledge of the geometrical properties of the ellipse corresponding to phase-cycled bSSFP signal allows us to estimate the central line, and therefore makes the constrained ellipse fitting formulation possible. Since we incorporate the central line information and knowledge of vertical ellipse into the problem, size of the parameter vector is reduced from 6 to 3. But, at least 4 phase-cycled acquisitions are required in our technique

as we need to find the cross-point of the ellipse as a first step. We improve the scan efficiency by reducing the number of phase-cycles required for T_1 and T_2 estimations, and similar estimation quality is obtained with fewer number of acquisitions compared to PLANET. We also successfully find the banding-free images and calculate the off-resonance maps. We perform in vivo experiments for brain imaging, but our simulations with various tissues in other body parts suggest that proposed method can be extended for imaging of other body parts. Also, this study can help to increase clinical utility of bSSFP, since it eliminates the off-resonance sensitivity in bSSFP images by providing banding-free image magnitudes, and the nonstandard contrast in bSSFP images by estimating quantitative maps which then can be used for synthesizing different image contrasts such as T1-weighted, T2-weighted images. This study can be further extended by investigating the effect of motion during the scan. Also, effects of acceleration schemes on the proposed method can be a subject of future study. Proposed method can be improved by acquiring more phase-cycled data as much as it is accelerated such that overall scan time remains same.

Bibliography

[1] B. Hargreaves, "Rapid gradient-echo imaging," *Journal of Magnetic Resonance Imaging*, vol. 36, no. 6, pp. 1300–1313, 2012.

[2] K. Scheffler and S. Lehnhardt, "Principles and applications of balanced SSFP techniques," *European radiology*, vol. 13, no. 11, pp. 2409–2418, 2003.

[3] M. L. Lauzon and R. Frayne, "Analytical characterization of rf phase-cycled balanced steady-state free precession," *Concepts in Magnetic Resonance Part A: An Educational Journal*, vol. 34, no. 3, pp. 133–143, 2009.

[4] M. A. Bernstein, K. F. King, and X. J. Zhou, *Handbook of MRI pulse sequences*. Elsevier, 2004.

[5] J. Lee, M. Lustig, D.-h. Kim, and J. M. Pauly, "Improved shim method based on the minimization of the maximum off-resonance frequency for balanced steady-state free precession (bssfp)," *Magnetic Resonance in Medicine: An Official Journal of the International Society for Magnetic Resonance in Medicine*, vol. 61, no. 6, pp. 1500–1506, 2009.

[6] T. Benkert, P. Ehses, M. Blaimer, P. M. Jakob, and F. A. Breuer, "Dynamically phase-cycled radial balanced SSFP imaging for efficient banding removal," *Magnetic resonance in medicine*, vol. 73, no. 1, pp. 182–194, 2015.

[7] A. Slawig, T. Wech, V. Ratz, J. Tran-Gia, H. Neubauer, T. Bley, and H. Köstler, "Multifrequency reconstruction for frequency-modulated b ssfp," *Magnetic resonance in medicine*, vol. 78, no. 6, pp. 2226–2235, 2017.

[8] K. H. Kim and S.-H. Park, "Artificial neural network for suppression of banding artifacts in balanced steady-state free precession mri," *Magnetic resonance imaging*, vol. 37, pp. 139–146, 2017.

[9] V. Roeloffs, S. Rosenzweig, H. C. M. Holme, M. Uecker, and J. Frahm, "Frequency-modulated ssfp with radial sampling and subspace reconstruction: A time-efficient alternative to phase-cycled bssfp," *Magnetic Resonance in Medicine*, vol. 81, no. 3, pp. 1566–1579, 2019.

[10] N. K. Bangerter, B. A. Hargreaves, S. S. Vasanawala, J. M. Pauly, G. E. Gold, and D. G. Nishimura, "Analysis of multiple-acquisition SSFP," *Magnetic resonance in medicine*, vol. 51, no. 5, pp. 1038–1047, 2004.

[11] T. Çukur, N. K. Bangerter, and D. G. Nishimura, "Enhanced spectral shaping in steady-state free precession imaging," *Magnetic resonance in medicine*, vol. 58, no. 6, pp. 1216–1223, 2007.

[12] A. M. Elliott, M. A. Bernstein, H. A. Ward, J. Lane, and R. J. Witte, "Nonlinear averaging reconstruction method for phase-cycle SSFP," *Magnetic resonance imaging*, vol. 25, no. 3, pp. 359–364, 2007.

[13] T. Çukur, M. Lustig, and D. G. Nishimura, "Multiple-profile homogeneous image combination: Application to phase-cycled SSFP and multicoil imaging," *Magnetic resonance in medicine*, vol. 60, no. 3, pp. 732–738, 2008.

[14] M. Björk, R. R. Ingle, E. Gudmundson, P. Stoica, D. G. Nishimura, and J. K. Barral, "Parameter estimation approach to banding artifact reduction in balanced steady-state free precession," *Magnetic resonance in medicine*, vol. 72, no. 3, pp. 880–892, 2014.

[15] Q.-S. Xiang and M. N. Hoff, "Banding artifact removal for bSSFP imaging with an elliptical signal model," *Magnetic resonance in medicine*, vol. 71, no. 3, pp. 927–933, 2014.

[16] M. N. Hoff, J. B. Andre, and Q.-S. Xiang, "Combined geometric and algebraic solutions for removal of bSSFP banding artifacts with performance comparisons," *Magnetic resonance in medicine*, vol. 77, no. 2, pp. 644–654, 2017.

[17] T. Hilbert, D. Nguyen, J.-P. Thiran, G. Krueger, T. Kober, and O. Bieri, "True constructive interference in the steady state (trueCISS)," *Magnetic resonance in medicine*, vol. 79, no. 4, pp. 1901–1910, 2018.

[18] O. Bieri and K. Scheffler, "Fundamentals of balanced steady state free precession mri," *Journal of Magnetic Resonance Imaging*, vol. 38, no. 1, pp. 2–11, 2013.

[19] N. K. Bangerter, T. Cukur, B. A. Hargreaves, B. S. Hu, J. H. Brittain, D. Park, G. E. Gold, and D. G. Nishimura, "Three-dimensional fluid-suppressed T2-prep flow-independent peripheral angiography using balanced SSFP," *Magnetic resonance imaging*, vol. 29, no. 8, pp. 1119–1124, 2011.

[20] T. Çukur, A. Shimakawa, H. Yu, B. A. Hargreaves, B. S. Hu, D. G. Nishimura, and J. H. Brittain, "Magnetization-prepared IDEAL bSSFP: a flow-independent technique for noncontrast-enhanced peripheral angiography," *Journal of Magnetic Resonance Imaging*, vol. 33, no. 4, pp. 931–939, 2011.

[21] E. Ilicak, S. Cetin, E. Bulut, K. K. Oguz, E. U. Saritas, G. Unal, and T. Çukur, "Targeted vessel reconstruction in non-contrast-enhanced steady-state free precession angiography," *NMR in Biomedicine*, vol. 29, no. 5, pp. 532–544, 2016.

[22] V. S. Deshpande, S. M. Shea, G. Laub, O. P. Simonetti, J. P. Finn, and D. Li, "3D magnetization-prepared true-FISP: a new technique for imaging coronary arteries," *Magnetic Resonance in Medicine: An Official Journal of the International Society for Magnetic Resonance in Medicine*, vol. 46, no. 3, pp. 494–502, 2001.

[23] H.-L. Margaret Cheng, N. Stikov, N. R. Ghugre, and G. A. Wright, "Practical medical applications of quantitative MR relaxometry," *Journal of Magnetic Resonance Imaging*, vol. 36, no. 4, pp. 805–824, 2012.

[24] J. Kim, H. Seo, S. So, and H. Park, "A multicontrast imaging method using steady-state free precession with alternating rf flip angles," *Magnetic resonance in medicine*, vol. 80, no. 4, pp. 1341–1351, 2018.

[25] S. C. Deoni, B. K. Rutt, and T. M. Peters, "Rapid combined T1 and T2 mapping using gradient recalled acquisition in the steady state," *Magnetic Resonance in Medicine: An Official Journal of the International Society for Magnetic Resonance in Medicine*, vol. 49, no. 3, pp. 515–526, 2003.

[26] S. C. Deoni, "Transverse relaxation time (T2) mapping in the brain with off-resonance correction using phase-cycled steady-state free precession imaging," *Journal of Magnetic Resonance Imaging: An Official Journal of the International Society for Magnetic Resonance in Medicine*, vol. 30, no. 2, pp. 411–417, 2009.

[27] K. Scheffler and J. Hennig, "T1 quantification with inversion recovery TrueFISP," *Magnetic Resonance in Medicine: An Official Journal of the International Society for Magnetic Resonance in Medicine*, vol. 45, no. 4, pp. 720–723, 2001.

[28] P. Schmitt, M. A. Griswold, P. M. Jakob, M. Kotas, V. Gulani, M. Flentje, and A. Haase, "Inversion recovery TrueFISP: quantification of T1, T2, and spin density," *Magnetic Resonance in Medicine: An Official Journal of the International Society for Magnetic Resonance in Medicine*, vol. 51, no. 4, pp. 661–667, 2004.

[29] P. Ehses, N. Seiberlich, D. Ma, F. A. Breuer, P. M. Jakob, M. A. Griswold, and V. Gulani, "Ir truefisp with a golden-ratio-based radial readout: fast quantification of t1, t2, and proton density," *Magnetic resonance in medicine*, vol. 69, no. 1, pp. 71–81, 2013.

[30] D. Ma, V. Gulani, N. Seiberlich, K. Liu, J. L. Sunshine, J. L. Duerk, and M. A. Griswold, "Magnetic resonance fingerprinting," *Nature*, vol. 495, no. 7440, p. 187, 2013.

[31] Y. Shcherbakova, C. A. van den Berg, C. T. Moonen, and L. W. Bartels, "PLANET: an ellipse fitting approach for simultaneous T1 and T2 mapping using phase-cycled balanced steady-state free precession," *Magnetic resonance in medicine*, vol. 79, no. 2, pp. 711–722, 2018.

[32] Y. Shcherbakova, C. A. van den Berg, C. T. Moonen, and L. W. Bartels, "On the accuracy and precision of PLANET for multiparametric MRI using phase-cycled bSSFP imaging," *Magnetic resonance in medicine*, vol. 81, no. 3, pp. 1534–1552, 2019.

[33] A. Fitzgibbon, M. Pilu, and R. B. Fisher, "Direct least square fitting of ellipses," *IEEE Transactions on pattern analysis and machine intelligence*, vol. 21, no. 5, pp. 476–480, 1999.

[34] R. Halır and J. Flusser, "Numerically stable direct least squares fitting of ellipses," in *Proc. 6th International Conference in Central Europe on Computer Graphics and Visualization. WSCG*, vol. 98, pp. 125–132, Citeseer, 1998.

[35] P. Waibel, J. Matthes, and L. Gröll, "Constrained ellipse fitting with center on a line," *Journal of Mathematical Imaging and Vision*, vol. 53, no. 3, pp. 364–382, 2015.

[36] J. Z. Bojorquez, S. Bricq, C. Acquitter, F. Brunotte, P. M. Walker, and A. Lalande, "What are normal relaxation times of tissues at 3 T?," *Magnetic resonance imaging*, vol. 35, pp. 69–80, 2017.

[37] N. Ben-Eliezer, D. K. Sodickson, and K. T. Block, "Rapid and accurate T2 mapping from multi–spin-echo data using Bloch-simulation-based reconstruction," *Magnetic resonance in medicine*, vol. 73, no. 2, pp. 809–817, 2015.

[38] L. I. Sacolick, F. Wiesinger, I. Hancu, and M. W. Vogel, "B1 mapping by Bloch-Siegert shift," *Magnetic resonance in medicine*, vol. 63, no. 5, pp. 1315–1322, 2010.

[39] Y. Shcherbakova, C. van den Berg, C. Moonen, and L. Bartels, "The influence of B0 drift on the performance of the PLANET method and an algorithm for correction," in *Proc 27th Annual Meeting ISMRM, Montreal*, p. 4608, 2019.